

Water Oxidation Catalysts

Synthesis and Physicochemical Properties of Ruthenium(II) Complexes Having Pentadentate Scaffolds: Water Oxidation Activity and Deactivation Pathway

Animesh Kundu,^[a] Srimoyee Khan,^[a] Subhasis Dey,^[a] Chiranjit Dutta,^[a] Anakuthil Anoop,^[a] and Sukanta Mandal*^[a]

Dedicated to Professor Rabindranath Mukherjee on the occasion of his 65th birthday

Abstract: Five mononuclear Ru^{II} complexes supported by two pentadentate polypyridyl ligands, *N,N*-bis(2-pyridylmethyl)-*N*-(bis-2-pyridylmethyl)amine (N₄Py) {[Ru(N₄Py)(Cl)](PF₆), **1^{Cl}**; [Ru(N₄Py)(OH₂)](PF₆)₂, **1^{Aq}**} and newly designed *N*-benzyl-*N*-((6-(6-methylpyridin-2-yl)pyridin-2-yl)methyl)dipyridin-2-yl-methanamine (N₂Py-MeBpy-Bz) {[Ru(N₂Py-MeBpy-Bz)(Cl)](PF₆)·MeCN, **2^{Cl}·MeCN**; [Ru(N₂Py-MeBpy-Bz)(OH₂)](PF₆)₂·3H₂O·MeOH, **2^{Aq}·3H₂O·MeOH** and [Ru(N₂Py-MeBpy-Bz)(MeCN)](PF₆)₂·0.5MeCN·H₂O, **2^{ACN}·0.5MeCN·H₂O**} were synthesized and characterized using different spectroscopic techniques such as UV/Vis, IR, 1D and 2D NMR spectroscopy, and mass spectrometry. The physicochemical properties of complexes **1^{Cl}** and **1^{Aq}**, and structural analysis of **1^{Aq}** were reported by Kojima and co-workers (*Chem. Sci.* **2012**, 3, 3421–3431). Structural characterizations

of **1^{Cl}**, **2^{Cl}·MeCN**, and **2^{ACN}·0.5MeCN·H₂O** were done by using single-crystal X-ray diffraction analyses. Catalytic water oxidation activities of aqua-ligated Ru^{II} complexes, using Ce^{IV} as sacrificial electron acceptor at pH 1, were examined. Complex **2^{Aq}** shows higher activity as compared to **1^{Aq}**. Electrochemical study suggests that a formal [Ru^{VI}=O]⁴⁺ species is the active species which triggers the oxidation of water. Mechanistic investigation reveals that O–O bond formation takes place via water nucleophilic attack (WNA) pathway. The deactivation pathway of catalyst **2^{Aq}** has also been investigated. It was observed that complex **2^{Aq}** lost its water oxidation activity primarily due to ligand degradation via oxidative *N*-debenzylation pathway.

Introduction

The economic growth all over the world has manifested in tremendous increase in energy demand compared with the last two decades. The world's energy supply majorly depends on carbon rich fossil fuels even in this century. Finding alternative to fossil fuels is urgently required for two major reasons: (i) their stocks are limited on the earth and (ii) continuous burning of them produces environmentally hazardous substances such as CO₂ gas which is considered as the major contributor to the global warming. The urgent need to reduce the CO₂ level in air has been accepted by scientists and political leaders of various nations as documented in Paris agreement during December 2015.^[1] Therefore the development of sustainable as well as environmentally friendly energy system is much needed for our future. In this context, the development of artificial photosystem which splits water into hydrogen and oxygen using sunlight would be one of the potential solutions of world's energy problem.^[2] From electrochemical point of view, the water split-

ting can be divided into two half redox reactions: oxidation of water (anode reaction: 2H₂O → O₂ + 4H⁺ + 4e⁻; E° = 1.23 V vs. NHE at pH = 0) and reduction of protons (cathode reaction: 4H⁺ + 4e⁻ → 2H₂; E° = 0.0 V vs. NHE at pH = 0). The water oxidation step in artificial photosynthesis is complicated as it involves multiple protons and electrons transfer and formation of an oxygen–oxygen bond. The high energy thermodynamics along with over potential present in reality make the oxidation step even more challenging.^[3] Beside the thermodynamic difficulties of the water oxidation step, the stability of water oxidation catalyst (WOC) under highly oxidizing condition is also seriously challenged as catalysts lost activity due to decomposition.^[4] Thus more investigation is required to understand the reaction mechanism of the water oxidation step and possible deactivation pathways that derail the system to cause decomposition to develop efficient artificial photosystem device for useful conversion and storage of solar energy into high-energy chemicals such as H₂.

After the first report of molecular WOC, *cis,cis*-[(bpy)₂-(H₂O)Ru^{III}ORu^{III}(OH₂)(bpy)₂](ClO₄)₄ (the “blue dimer”, bpy = 2,2'-bipyridine),^[5] by Meyer et al. in 1982, several WOCs based on rare earth (Ru, Ir)^[3] and earth abundant^[6] first row transition metal ions have been developed and studied. Although Ru is rare on earth and thus expensive, Ru-based complexes have attracted much attention towards researchers because of their

[a] Department of Chemistry, Indian Institute of Technology Kharagpur, Kharagpur 721302, India

E-mail: sukanta.mandal@chem.iitkgp.ac.in

http://www.iitkgp.ac.in/departement/CY/faculty/cy-sukanta.mandal

Supporting information and ORCID(s) from the author(s) for this article are available on the WWW under <https://doi.org/10.1002/ejic.201801099>.

superior performance and higher stability under oxidizing condition.^[3,7] The 1st row transition metal ions, being kinetically labile in general, often undergo easy ligand decoordination/hydrolysis in aqueous medium and thus lose the molecular nature very easily.^[8] This leads to the formation of metal oxides/hydroxides nanoparticles which generally exhibit catalytic activity; therefore, the characterization of the active species and mechanistic investigations with these complexes become more complicated.^[9] However, ruthenium, being a 4d element, nicely keeps the balance between kinetic lability and inertness and maintains the molecular nature at a very wide range of pH.

One of the criteria for a metal complex to promote water oxidation catalysis is that it should acquire adequate oxidation potential by forming a high-valent metal-oxo species. Therefore, the ligand having high electron donating ability would be a judicious choice to design a catalyst for the easy access of metal ions at higher oxidation state.^[10] The Ru-aqua polypyridyl complexes are particularly interesting because they can access high oxidation states and form Ru-oxo species via proton-coupled electron transfer (PCET) pathway at a narrow potential gap, and thereby reduce the over potential to a large extent.^[11] The pentadentate-polypyridyl transition metal complexes show interesting oxidative properties,^[12–15] including water oxidation.^[16–18] The pentadentate scaffold has few advantages: (i) it ensures the binding with metal ion in square pyramidal fashion so that one coordination site become free to accommodate aqua ligand in order to attain an octahedral geometry, thus facilitating PCET processes; (ii) it enhances the stability of metal complexes due to chelate effect, thus preventing decomposition via ligand decoordination; and (iii) it enhances the σ -donating property due to its inherent rigidity which might help in accessing the high-valent state.

Researchers have emerged taking advantage of the interesting properties of the pentadentate scaffold of *N,N*-bis(2-pyridylmethyl)-*N*-(bis-2-pyridylmethyl)amine (N_4Py) ligand to characterize the high-valent metal-oxo species with Fe^[13] and Mn.^[14] The Ru complex with N_4Py ligand, $[Ru(N_4Py)(OH_2)](PF_6)_2$ (**1^{Aq}**) was shown to undergo PCET process to generate high-valent Ru=O species which catalyzed the oxidation of alcohols and olefins.^[15] Motivated by the interesting oxidation chemistry of metal ions with pentadentate scaffold of N_4Py ligand, we have designed a new pentadentate ligand, *N*-benzyl-*N*-((6-(6-methylpyridin-2-yl)pyridin-2-yl)methyl)dipyridin-2-yl-methanamine (N_2Py -^{Me}Bpy-Bz). Here in, we report the syntheses and characterizations of Ru^{II} complexes: $[Ru(N_2Py$ -^{Me}Bpy-Bz)(Cl)](PF₆)·MeCN, **2^{Cl}**·MeCN; $[Ru(N_2Py$ -^{Me}Bpy-Bz)(OH₂)](PF₆)₂·3H₂O·MeOH, **2^{Aq}**·3H₂O·MeOH and $[Ru(N_2Py$ -^{Me}Bpy-Bz)(MeCN)](PF₆)₂·0.5MeCN·H₂O, **2^{ACN}**·0.5MeCN·H₂O (Figure 1). We are interested in exploring the chemically driven water oxidation with complexes **1^{Aq}** and **2^{Aq}** (Figure 1). Complex **2^{Aq}** shows higher activity than **1^{Aq}**. The presence of a bipyridyl moiety in the pentadentate ligand architecture improves the reactivity. Electrochemical and kinetic analysis suggest water oxidation at single-site of Ru where O–O bond formation proceeds via formal ruthenium(VI)-oxo intermediate. This differs from other reported polypyridyl based Ru complexes where Ru^V state is the active intermediate.^[11d,17,19] The deactivation process of catalyst **2^{Aq}**

has also been studied. Mass spectroscopic studies aimed at intercepting possible decomposition products revealed that ligand degradation via oxidative *N*-debenzylation pathway primarily derailed complex **2^{Aq}** from its water oxidation activity. Thus these studies might provide new mechanistic insights towards water oxidation through ruthenium(VI)-oxo intermediate as well as the possible deactivation pathway which might help to come up better design of catalyst for optimum performance.

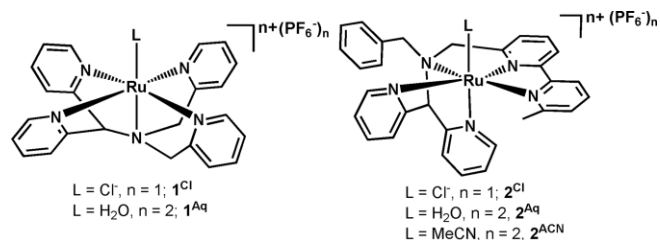


Figure 1. Mononuclear Ru^{II} complexes discussed in this work.

Results and Discussion

Design, Syntheses of Ligands and Ru^{II} Complexes and Characterizations

The pentadentate ligand N_4Py has attracted much attention to researchers because of its unique property to generate active metal-oxo species for oxidative reactions.^[13–15] The rigidity imposed by the di-2-pyridylmethanamine moiety increases the σ -donating ability, thus stabilizes the high-valent state. Therefore, we became interested to explore the water oxidation by high-valent ruthenium-oxo species with ligands having di-2-pyridylmethanamine moiety. In this context, we have chosen reported^[15] N_4Py ligand and developed a new pentadentate mononucleating chelating ligand, N_2Py -^{Me}Bpy-Bz, having di-2-pyridylmethanamine and bipyridyl moieties. The pentadentate scaffolds have been judiciously chosen to ensure an aqua ligation at the vacant site so that the high-valent ruthenium-oxo species would be generated via PCET process.

The Ru^{II} complexes, **1^{Cl}** and **1^{Aq}** were synthesized by following the literature method and the physicochemical properties (see experimental section and Figures S1–S5 in the Supporting Information) of both the complexes agreed with that described in the literature.^[15] The complex **1^{Cl}** was further characterized by single-crystal X-ray crystallography. A perspective view of the cationic part of **1^{Cl}** is shown in Figure S6, with crystallographic parameters listed in Tables S1–S2, Supporting Information. As shown in Figure S6, the Ru^{II} center adopts a distorted octahedral geometry where five coordination sites are satisfied by pentadentate N_4Py ligand and the sixth position is occupied by Cl⁻ ion. The chloride and the tertiary amine nitrogen are in *trans* position. The basic structural features (i.e. bond lengths, bond angles) of **1^{Cl}** resemble very closely with its aqua analogue, **1^{Aq}**.^[15]

The new ligand N_2Py -^{Me}Bpy-Bz was synthesized in a multi-step synthetic procedure. The Schiff base condensation between di-2-pyridylmethanamine^[20a] and 6'-methyl-2,2'-bipyridine-6-carbaldehyde^[20b] and further reduction with NaBH₄

yielded *N*-((6-(6-methylpyridin-2-yl)pyridin-2-yl)methyl)-di-pyridin-2-yl-methanamine ($N_2Py\text{-}^{Me}Bpy$). Treatment of $N_2Py\text{-}^{Me}Bpy$ with benzyl chloride in presence of *N,N*-diisopropylethylamine yielded the final ligand $N_2Py\text{-}^{Me}Bpy\text{-}Bz$. The ligands were characterized by NMR spectroscopy (Figures S7, S8). The reaction of $N_2Py\text{-}^{Me}Bpy\text{-}Bz$ with *cis*-[Ru(DMSO)₄Cl₂]^[20c] in methanol under inert atmosphere resulted a new chloro-ligated mononuclear Ru complex, [Ru($N_2Py\text{-}^{Me}Bpy\text{-}Bz$)(Cl)](PF₆) (**2^{Cl}**). The complex **2^{Cl}** was formed in a molecular self-assembly process, by stepwise replacement of labile DMSO and Cl⁻ of *cis*-[Ru(DMSO)₄Cl₂] with ligand under refluxing condition. Recrystallization of **2^{Cl}** from acetonitrile afforded analytically pure complex **2^{Cl}·MeCN**. The synthesis of aqua-ligated complex, [Ru($N_2Py\text{-}^{Me}Bpy\text{-}Bz$)(OH₂)](PF₆)₂·3H₂O·MeOH (**2^{Aq}·3H₂O·MeOH**) was accomplished by treating **2^{Cl}** with AgPF₆ in methanol/water mixture under refluxing condition. An acetonitrile coordinated complex was obtained during recrystallization of **2^{Aq}·3H₂O·MeOH** from MeCN solvent. Since MeCN is stronger donating ligand than aqua, H₂O can easily be replaced by MeCN to form the complex [Ru($N_2Py\text{-}^{Me}Bpy\text{-}Bz$)(MeCN)](PF₆)₂·0.5MeCN·H₂O (**2^{ACN}·0.5MeCN·H₂O**). Elemental analysis data are in good agreement with the above formulations for all three new Ru^{II} complexes. All three new complexes have been characterized by various spectroscopic techniques. Further, X-ray diffraction analyses have been carried out for **2^{Cl}·MeCN** and **2^{ACN}·0.5MeCN·H₂O** complexes (see below).

IR spectrum of **2^{Aq}** displayed broad absorption due to $\nu(O-H)$ of water at ca. 3450 cm⁻¹. A weak absorption at ca. 2250 cm⁻¹ due to the $\nu(C\equiv N)$ stretching vibration of coordinated acetonitrile was observed for complex **2^{ACN}**. All three complexes displayed an intense IR absorption at ≈ 840 cm⁻¹, due to the presence of PF₆⁻ counter anion. The MALDI-MS spectra authenticated the formation of metal-ligand complex (Figures S9, S10).

The UV/Vis spectra of **2^{Cl}** (in MeCN), **2^{Aq}** (in 0.1 M aqueous CF₃SO₃H) and **2^{ACN}** (in MeCN) are displayed in Figures S11, Figure S12 and Figure S13, respectively. As expected, two types of charge-transfer bands [MLCT: Ru(*d* π) \rightarrow ligand(*p* π^*) and LLCT: ligand(*p* π) \rightarrow ligand(*p* π^*)] are observed for all three Ru^{II} complexes.^[11b,11f,17] For complex **2^{Cl}** the two MLCT bands are observed at 509 nm and 353 nm along with two intense LLCT bands in the near-UV region at 302 and 251 nm. The MLCT band of complex **2^{Aq}** was shifted to 467 nm which is consistent with the replacement of a weak-field Cl⁻ ion with a water molecule.^[17b] The two intense LLCT transitions for **2^{Aq}** were observed at 297 and 248 nm. The MLCT and LLCT bands of **2^{ACN}** were observed at 437, 397 nm and 291, 254 nm, respectively. As seen from the UV/Vis spectra a significant shift in the position of MLCT bands were observed for all three complexes, indicating that the π -acceptor character of the pentadentate ligand varies with substitution of monodentate ligand from Cl⁻ to H₂O to MeCN.

As Ru^{II} complexes are diamagnetic, complexes **2^{Cl}**, **2^{Aq}** and **2^{ACN}** were also characterized by 1D and 2D NMR spectroscopy (Figures S14–S18). The chemical shift values are listed in corresponding experimental section. Few features are noticeable in ¹H NMR spectra: (i) the predominating tendency is for a down-

field shift of ¹H resonances upon coordination to the positively charged metal ion (coordination-induced shift), (ii) the methylene protons and methine proton appear as singlet, as observed with free ligand, however, (iii) for the methylene protons [CH₂Ph & CH₂(Bpy)] four doublet signals for **2^{Cl}** [CH₂Ph: 3.27 & 4.16 ppm, *J* = 15.2 Hz; CH₂(Bpy): 3.74 & 4.52 ppm, *J* = 17.6 Hz] and **2^{ACN}** [CH₂Ph: 3.45 & 4.17 ppm, *J* = 14.4 Hz; CH₂(Bpy): 3.85 & 4.76 ppm, *J* = 18.0 Hz]; whereas two doublet & one multiplet (overlap of two resonances) signals for **2^{Aq}** [3.39 (*d*, 1 H, *J* = 14.4 Hz), 3.78–3.87 (*m*, 2 H), 4.60 (*d*, 1 H, *J* = 17.6 Hz)] are observed – attesting the fact that each methylene proton became magnetically non-equivalent after complexation, (iv) among two pyridyl moieties, the H6 proton of the pyridine group which is *trans* to the Cl⁻/H₂O/MeCN resonates at the most downfield in the corresponding complexes **2^{Cl}**: 9.60 (*d*, 1 H, *J* = 5.2 Hz); **2^{Aq}**: 9.50 (*d*, 1 H, *J* = 8 Hz); **2^{ACN}**: 9.51 (*d*, 1 H, *J* = 5.2 Hz)]. Few noticeable changes in ¹³C NMR for **2^{Cl}** and **2^{ACN}** are observed as well compared with the free ligand (Figures S8, S15, S18). For instance, the two methylene carbons [CH₂Ph & CH₂(Bpy)] resonate at same position (δ = 39.95 ppm) in case of free ligand, where as they resonate at two different positions in metal complex [CH₂Ph: 58.38 (**2^{Cl}**), 59.17 (**2^{ACN}**); CH₂(Bpy): 60.92 (**2^{Cl}**), 61.25 (**2^{ACN}**)].

Transformation of **2^{Aq}** to **2^{ACN}** (NMR and UV/Vis Study)

The transformation of **2^{Aq}** \rightarrow **2^{ACN}** was observed when the ¹H NMR spectrum of **2^{Aq}** was recorded in CD₃CN. The Figure 2 depicts the spectral-change when **2^{Aq}** was dissolved in CD₃CN. A benchmark used in the analysis of NMR spectra was the methine proton of di-2-pyridyl moiety. The gradual loss of singlet peak of methine proton at δ = 6.09 ppm for **2^{Aq}** with concurrent evolution of new singlet at δ = 6.15 ppm indicates the substitution of bound H₂O with CD₃CN. Within an hour $\approx 36\%$ **2^{ACN}** was formed (Figure 2 bottom); and in prolonged time (≈ 12 h) a clean progression to a single acetonitrile-coordinated product (**2^{ACN}**) was observed (Figure 2 top).

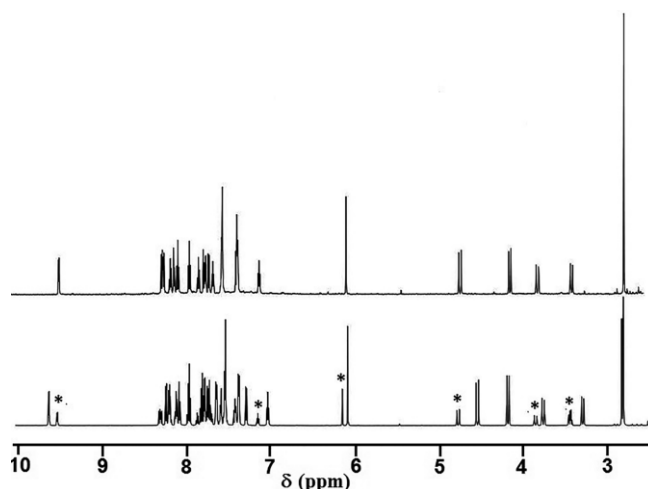


Figure 2. ¹H NMR (600 MHz, 300 K) spectral-change during the course of transformation of complex **2^{Aq}** to **2^{ACN}**: (bottom) after 1 hr of sample preparation [few signals for **2^{ACN}** are marked with *]; (top) after 12 h of sample preparation. Sample was prepared by dissolving **2^{Aq}** in CD₃CN.

The substitution process of labile aqua by MeCN for **2^{Aq}** was further monitored by UV/Vis spectroscopy. As shown in Figure 3, upon addition of excess acetonitrile into an aqueous (CF₃SO₃H, pH 1) solution of **2^{Aq}** the MLCT band with λ_{max} at 467 nm is progressively blue-shifted to 437 nm with isosbestic point at 446 nm. This finding corroborated the formation of acetonitrile-coordinated complex, as the final spectra obtained resembles with that of isolated **2^{ACN}** shown in Figure S13. The appearance of isosbestic point indicates a clean transformation of complex **2^{Aq}** to **2^{ACN}**. The substitution kinetics were measured under pseudo first order condition with excess acetonitrile. A plot of first-order rate constant (k_{obs}) vs. [MeCN] was linear passing through the origin, revealing a first-order dependence of the rate on the concentration of acetonitrile and from the slope the overall second-order rate constant was determined to be $3.05 \times 10^{-2} \text{ M}^{-1} \text{ s}^{-1}$ at 30 °C (Figure S19).

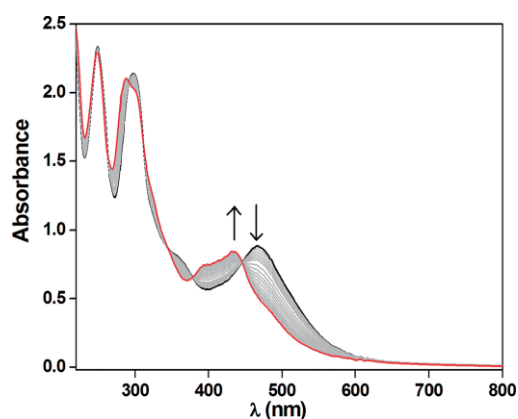


Figure 3. A representative UV/Vis spectral-change over time after addition of MeCN into an aqueous CF₃SO₃H acid solution (pH 1) of **2^{Aq}** at 30 °C. [**2^{Aq}**] = 0.100 mM; [MeCN] = 0.255 M. The black line represents the initial spectrum of **2^{Aq}** prior MeCN addition; and red line represents final spectrum. Arrow indicates absorption change.

Description of Structures

(a) [Ru(N₂Py-MeBpy-Bz)(Cl)](PF₆)-MeCN (**2^{Cl}-MeCN**)

The complex was crystallized into a monoclinic lattice with the space group of *Pc* (#7). The asymmetric unit consists of two [Ru(N₂Py-MeBpy-Bz)(Cl)]⁺ units, two PF₆ ions as counter anions, and two MeCN molecule as a solvent of crystallization; therefore the formula for one unit is represented as [Ru(N₂Py-MeBpy-Bz)(Cl)](PF₆)-MeCN (**2^{Cl}-MeCN**). The two units are discriminated by use of suffixes "a" & "b" for atoms corresponding to the donor atoms coordinate to for Ru(1) and Ru(2), respectively. A perspective view of the cationic part of complex **2^{Cl}-MeCN** (for unit corresponds to Ru(1)) is shown in Figure 4 and selected bond lengths and bond angles for both the units are displayed in Table 1. The six coordination of Ru^{II} center is satisfied by five nitrogen donor atoms from the ligand and chloride ion. The chloride ion Cl(1a/1b) and one of the pyridine-N atom, N(1a/1b) of di-2-pyridyl moiety are *trans* to each other. The Ru-N_x (x = 1a/1b, 2a/2b, 3a/3b) bond lengths are in a normal range (average distance = 2.083 Å),^[17a] however, one of the two Ru-N bonds of bipyridyl moiety is relatively shorter [Ru(1/2)-

N(4a/4b) = 1.950(5) Å (average)] while the other bond is longer [Ru(1/2)-N(5a/5b) = 2.116(5) Å (average)] compared to other Ru-N_x (x = 1a/1b, 2a/2b, 3a/3b) distances, due to strain imposed in the ligand framework. Among two Ru-N(pyridine) distances, the Ru(1/2)-N(1a/1b) bond length [2.042(5) Å (average)], which is *trans* to the chloride ion, is shorter than other Ru(1/2)-N(2a/2b) distances [2.1075(6) Å (average)]. The Ru-Cl distance [2.4564 Å (average)] is slightly longer than that in **1^{Cl}** but shorter than those reported in literature.^[17a] The Ru center is deviated from the mean planes consisting of N1-N2-Cl-N4, N1-N3-Cl-N5 and N2-N3-N4-N5 with the distance of 0.1598, 0.1308 and 0.0142 Å (average value of the corresponding plane of two units), respectively. The equatorial bond angles around Ru center largely deviates from the ideal 90° and the axial bond angles are shorter than 180°, implying that the structure is highly distorted. The dihedral angles of bipyridine and N2-pyridine rings with N2-N3-N4-N5 plane are 18.414° and 28.907°

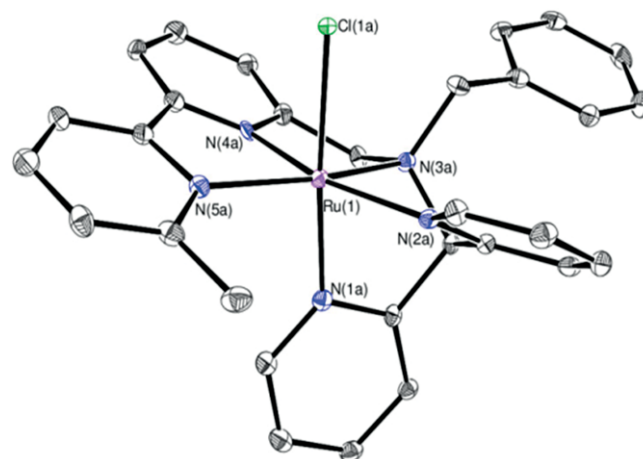


Figure 4. ORTEP (30%) view of the metal coordination environment in the crystal of [Ru(N₂Py-MeBpy-Bz)(Cl)](PF₆)-MeCN (**2^{Cl}-MeCN**). Only donor atoms are labeled. Hydrogen atoms are omitted for clarity.

Table 1. Selected bond lengths (Å) and angles (°) of [Ru(N₂Py-MeBpy-Bz)(Cl)](PF₆)-MeCN (**2^{Cl}-MeCN**).

Ru(1)-N(1a)	2.043(5)	Ru(2)-N(1b)	2.041(5)
Ru(1)-N(2a)	2.113(6)	Ru(2)-N(2b)	2.102(6)
Ru(1)-N(3a)	2.094(5)	Ru(2)-N(3b)	2.107(5)
Ru(1)-N(4a)	1.957(5)	Ru(2)-N(4b)	1.943(5)
Ru(1)-N(5a)	2.121(5)	Ru(2)-N(5b)	2.111(5)
Ru(1)-Cl(1a)	2.4464(15)	Ru(2)-Cl(1b)	2.4664(15)
N(1a)-Ru(1)-N(4a)	96.9(2)	N(1b)-Ru(2)-N(4b)	95.4(2)
N(3a)-Ru(1)-N(4a)	84.8(2)	N(3b)-Ru(2)-N(4b)	84.4(2)
N(1a)-Ru(1)-N(3a)	80.8(2)	N(1b)-Ru(2)-N(3b)	80.3(2)
N(1a)-Ru(1)-N(2a)	84.9(2)	N(1b)-Ru(2)-N(2b)	85.9(2)
N(2a)-Ru(1)-N(3a)	79.81(19)	N(2b)-Ru(2)-N(3b)	80.3(2)
N(4a)-Ru(1)-N(5a)	77.9(2)	N(4b)-Ru(2)-N(5b)	77.7(2)
N(1a)-Ru(1)-N(5a)	98.3(2)	N(1b)-Ru(2)-N(5b)	98.6(2)
N(2a)-Ru(1)-N(5a)	117.6(2)	N(2b)-Ru(2)-N(5b)	117.7(2)
N(2a)-Ru(1)-N(4a)	164.0(2)	N(2b)-Ru(2)-N(4b)	164.2(2)
N(3a)-Ru(1)-N(5a)	162.5(2)	N(3b)-Ru(2)-N(5b)	161.9(2)
N(1a)-Ru(1)-Cl(1a)	175.41(15)	N(1b)-Ru(2)-Cl(1b)	175.92(15)
N(2a)-Ru(1)-Cl(1a)	90.71(16)	N(2b)-Ru(2)-Cl(1b)	90.41(16)
N(3a)-Ru(1)-Cl(1a)	97.11(15)	N(3b)-Ru(2)-Cl(1b)	97.40(15)
N(4a)-Ru(1)-Cl(1a)	86.90(16)	N(4b)-Ru(2)-Cl(1b)	87.73(17)
N(5a)-Ru(1)-Cl(1a)	84.93(15)	N(5b)-Ru(2)-Cl(1b)	84.59(15)

(average value of two units), respectively. Due to this tilting the π -back bonding from the Ru center to the pyridine rings does not occur effectively and consequently the Lewis acidity of the Ru center should increase.

(b) [Ru(N₂Py-MeBpy-Bz)(MeCN)](PF₆)₂·0.5MeCN·H₂O (2^{ACN}·0.5MeCN·H₂O)

The complex was crystallized into a triclinic lattice with the space group of $P\bar{1}$ (#2). The asymmetric unit contains a pair of enantiomeric [Ru(N₂Py-MeBpy-Bz)(MeCN)]²⁺ unit, four PF₆ ions as counter anions, and one MeCN & two H₂O molecules as

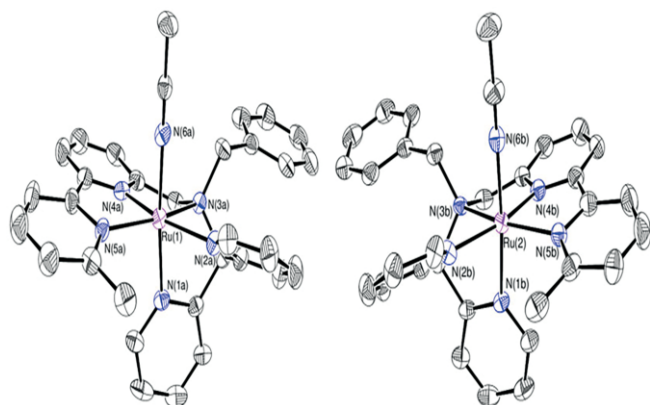


Figure 5. ORTEP (30 %) view of the metal coordination environment of the pair of enantiomers in the crystal of [Ru(N₂Py-MeBpy-Bz)(MeCN)](PF₆)₂·0.5MeCN·H₂O (**2^{ACN}·0.5 MeCN·H₂O**). Only donor atoms are labelled. Hydrogen atoms are omitted for clarity.

Table 2. Selected bond lengths (Å) and angles (°) of [Ru(N₂Py-MeBpy-Bz)(MeCN)](PF₆)₂·0.5MeCN·H₂O (**2^{ACN}·0.5MeCN·H₂O**).

Ru(1)–N(1a)	2.065(5)	Ru(2)–N(1b)	2.044(5)
Ru(1)–N(2a)	2.123(5)	Ru(2)–N(2b)	2.110(5)
Ru(1)–N(3a)	2.082(5)	Ru(2)–N(3b)	2.080(5)
Ru(1)–N(4a)	1.970(5)	Ru(2)–N(4b)	1.943(5)
Ru(1)–N(5a)	2.130(5)	Ru(2)–N(5b)	2.134(5)
Ru(1)–N(6a)	2.040(6)	Ru(2)–N(6b)	2.038(6)
N(1a)–Ru(1)–N(2a)	86.4(2)	N(1b)–Ru(2)–N(2b)	86.7(2)
N(1a)–Ru(1)–N(3a)	80.1(2)	N(1b)–Ru(2)–N(3b)	80.2(2)
N(1a)–Ru(1)–N(4a)	92.3(2)	N(1b)–Ru(2)–N(4b)	92.0(2)
N(1a)–Ru(1)–N(5a)	97.4(2)	N(1b)–Ru(2)–N(5b)	96.8(2)
N(1a)–Ru(1)–N(6a)	174.5(2)	N(1b)–Ru(2)–N(6b)	175.2(2)
N(2a)–Ru(1)–N(3a)	79.7(2)	N(2b)–Ru(2)–N(3b)	79.8(2)
N(2a)–Ru(1)–N(4a)	164.2(2)	N(2b)–Ru(2)–N(4b)	164.1(2)
N(2a)–Ru(1)–N(5a)	118.4(2)	N(2b)–Ru(2)–N(5b)	117.5(2)
N(2a)–Ru(1)–N(6a)	88.7(2)	N(2b)–Ru(2)–N(6b)	90.1(2)
N(3a)–Ru(1)–N(4a)	84.6(2)	N(3b)–Ru(2)–N(4b)	84.5(2)
N(3a)–Ru(1)–N(5a)	161.7(2)	N(3b)–Ru(2)–N(5b)	162.5(2)
N(3a)–Ru(1)–N(6a)	96.5(2)	N(3b)–Ru(2)–N(6b)	95.7(2)
N(4a)–Ru(1)–N(5a)	77.4(2)	N(4b)–Ru(2)–N(5b)	78.4(2)
N(4a)–Ru(1)–N(6a)	91.6(2)	N(4b)–Ru(2)–N(6b)	90.0(2)
N(5a)–Ru(1)–N(6a)	87.2(2)	N(5b)–Ru(2)–N(6b)	87.9(2)

Table 3. Summary of the deprotonation constants and redox potentials of Ru^{II}-OH₂ complexes.

Comp.	Ru ^{II} -OH ₂	Ru ^{III} -OH ₂	E _{1/2} , V vs. NHE at pH 1		
	pK _a	pK _a	Ru ^{III/II}	Ru ^{V/III}	Ru ^{VI/IV}
1^{Aq}	12.0 ^[14]	2.30 ^[b]	0.90	1.22	1.56
2^{Aq}	10.63 ^[a] (10.70) ^[b]	1.90 ^[b]	0.95	1.17	1.60

[a] Determined by spectrophotometric titration. [b] Determined from Pourbaix diagram.

solvent of crystallization; so the formula for one molecule is represented as [Ru(N₂Py-MeBpy-Bz)(MeCN)](PF₆)₂·0.5MeCN·H₂O (**2^{ACN}·0.5MeCN·H₂O**). The perspective view of the pair of enantiomers of [Ru(N₂Py-MeBpy-Bz)(MeCN)]²⁺ is displayed in Figure 5 and bond lengths and bond angles are listed in Table 2. As that of **2^{Cl}·MeCN**, the Ru^{II} center adopts distorted octahedral geometry and the basic structural features are unremarkable.

Acid Base Equilibria

The pK_a value for the aqua proton dissociation of complex **2^{Aq}** was determined by spectroscopic titration ranging from pH 0.40 to 12.50 using UV/Vis absorption spectroscopy. The sample solution for pH range of 0.40 < pH < 1.80 was prepared in an aqueous solution of CF₃SO₃H acid and the required pH was adjusted by adding neat CF₃SO₃H acid; whereas for higher pH domain 1.80 < pH < 12.70 Britton–Robinson (B.-R.) buffer was used and the pH was adjusted by addition of NaOH. As seen from Figure S20, no significant change in MLCT band was observed by varying the pH in the range pH = 0.40–8.50, indicating no deprotonation occurred in that pH domain. However, as the pH value rises from 8.50 to 12.70, the maximum absorption wave length for the MLCT band of **2^{Aq}** shows a red shift from 467 nm to 522 nm with a meaningful change in the molar absorptivity of the band, because of the increase in the donating property of the hydroxyl group resulted from the deprotonation of the originally coordinated aqua ligand, leading to the lowering in the MLCT transition energy. So on the basis of absorption changes in the pH range of 0.40–12.70, the deprotonation constant (pK_a) of the aqua ligand of complex **2^{Aq}** was determined to be 10.63 as depicted in Figure S20c. The pK_a value determined for **2^{Aq}** is consistent with other related Ru^{II}-OH₂ complexes.^[11f,17a,21] For complex **1^{Aq}** Kojima et al. reported two pK_a values^[15] for coordinated aqua ligand. As reported,^[15] in lower pH domain (pH 0.40–3.80) a slight red shift in the MLCT band with almost no change in the absorption intensity was observed. This small shift might happen due to the change in the dielectric constant which may induce a non-negligible shift in the MLCT band owing to the relatively large transition dipole originating upon excitation. So pK_{a1} = 1.85^[15] cannot be judged as first deprotonation constant of aqua coordinated to Ru^{II} center. Rather pK_{a2} = 12^[15] is likely to be correlated with pK_a of coordinated water for **1^{Aq}**. Notably, the pK_a of **2^{Aq}** is lower than **1^{Aq}**, implying the Ru center of **2^{Aq}** possesses greater Lewis acid character than **1^{Aq}** (Table 3).

Electrochemical Behavior

The redox behavior of Ru^{II}-OH₂ complexes has been investigated in aqueous media by cyclic voltammogram (CV) and square wave voltammogram (SWV) method. The CV and SWV

curves of 2^{Aq} are displayed in Figure 6. As seen from Figure 6b, the SWV curve of 2^{Aq} in acidic aqueous condition (pH 1, CF_3SO_3H) exhibits a sequence of three oxidative responses at 0.95, 1.17, and 1.60 V vs. NHE; whereas under nearly neutral aqueous condition (pH 6.85, B.-R. buffer) it exhibits three well shaped oxidative responses at 0.62, 0.77, and 1.17 along with barely visible wave at 1.60 V vs. NHE. In order to know the number of electron transfer involved in first two/three redox waves, controlled potential electrolysis (CPE) was carried out at respective pH. In acidic condition, pH 1 at 1.03 V vs. NHE (just after potential of first redox wave) a value of 0.95 electrons per complex molecule was obtained, while at 1.35 V vs. NHE (just after potential of second redox wave) a value of 3.20 electrons per complex molecule was obtained (Figure S21). Similarly, CPE analyses under neutral conditions (pH 6.85) at potential 0.65 (after first redox wave), 0.95 (after second redox wave), and 1.35 V (third redox wave) vs. NHE yielded a value of approximately one electron, two electrons, and three electrons per complex molecule, respectively. So briefly from an electronic point of view 2^{Aq} favors one-electron transfer between Ru^{II} , Ru^{III} and Ru^{IV} at higher pH domain; while under acidic condition it shows a tendency of one-electron and two-electron transfer for $Ru^{III/II}$ and $Ru^{V/III}$ processes, respectively (see Pourbaix diagram below). Therefore, the three redox signals observed at 0.95, 1.17, and 1.60 V vs. NHE at pH 1 can tentatively be assigned as $Ru^{III/II}$, $Ru^{V/III}$, $Ru^{VI/V}$ redox couple, respectively. The Ru^V and Ru^{VI} species are generated at lower applied potential as observed before for other Ru-compounds.^[22] The CV of 2^{Aq} at acid media (pH 1, CF_3SO_3H) shows a larger electro catalytic wave on onset potential at ≈ 1.50 V (Figure S22). This catalytic wave is associated to water oxidation catalysis, indicating complex 2^{Aq} is capable of oxidizing water. The Ru^{VI}/Ru^V redox potential lies on the onset of the catalytic wave, implying that the formal high-valent Ru^{VI} species is the active species responsible for the catalysis. Only few Ru-WOCs are reported in literature, where high-valent Ru^{VI} species have been proposed to be an active intermediate for water oxidation catalysis.^[22a,22b,23] The intriguing capability of accessing such a high valent Ru^{VI} state (due to the unique rigidity of the ligand and PCET process) distinguishes complex 2^{Aq} from other reported neutral polypyridyl based complexes where water oxidation was triggered via Ru^V intermediate.^[11d,17,19] Similar to complex 2^{Aq} , complex 1^{Aq} displayed three peaks at 0.90, 1.22 and 1.56 V vs. NHE in pH 1 CF_3SO_3H acid media and from CPE analysis these three waves can also be assigned as Ru^{III}/Ru^{II} , Ru^V/Ru^{III} and Ru^{VI}/Ru^V couples, respectively (Figure S23). The corresponding redox potentials of 1^{Aq} and 2^{Aq} are very much comparable (Table 3). This is expected because of similar N_5O -ligand environment for both the complexes. However, in CV diagram a dramatic difference in catalytic current was observed between the two complexes. As depicted in Figure S24, complex 2^{Aq} shows higher catalytic current, whereas complex 1^{Aq} shows marginal current with respect to blank voltammogram. This finding suggests superior water oxidation activity of 2^{Aq} compared to 1^{Aq} .

The Pourbaix diagram of complex 2^{Aq} in the region of pH 0.48–11.52 (Figure 7) provides more comprehensive insights into the electrochemical properties and redox compositions depending on the potential and pH of the medium (Figure S25). From pK_a value of 2^{Aq} it is evident that complex exists as $[Ru^{II}-OH_2]^{2+}$ form at lower pH condition. In region $1.85 < pH < 10.56$, the redox potential of Ru^{III}/Ru^{II} couple decreases linearly with a slope of -58 mV/pH. This phenomenon can be ascribed as typical one-electron and one-proton ($1e^-$, $1H^+$) PCET process for $[Ru^{III}-OH]^{2+}/[Ru^{II}-OH_2]^{2+}$ redox couple. In the region of $pH > 10.56$ and $pH < 1.85$, the Ru^{III}/Ru^{II} redox potential becomes pH independent, reflecting only one-electron transfer process for redox couples $[Ru^{III}-OH]^{2+}/[Ru^{II}-OH]^+$ and $[Ru^{III}-OH_2]^{3+}/[Ru^{II}-OH_2]^{2+}$, respectively. Therefore, from Pourbaix diagram the pK_a of $[Ru^{II}(N_2Py-MeBpy-Bz)(OH_2)]^{2+}$ is estimated to be 10.70, which agrees very well with the result obtained from spectrophotometric titration (Table 3), and the pK_a of $[Ru^{III}(N_2Py-MeBpy-Bz)(OH_2)]^{3+}$ is determined to be 1.90. The Ru^{IV}/Ru^{III} redox couple was observed at higher pH domain $11.52 < pH < 2.35$ (vide supra) and the redox potential decreases linearly with increase of pH with a slope of -58 mV/pH, attesting ($1e^-$, $1H^+$) PCET process for $[Ru^{IV}=O]^{2+}/[Ru^{III}-OH]^{2+}$ redox couple. However, the Ru^{IV}/Ru^{III} redox couple was not observed at stronger acidic region ($0.48 < pH < 2.35$), instead we indeed observed formation of Ru^V species from Ru^{III} (vide supra). So apparently Ru^{IV} oxidation state might be a missing state in lower pH domain,

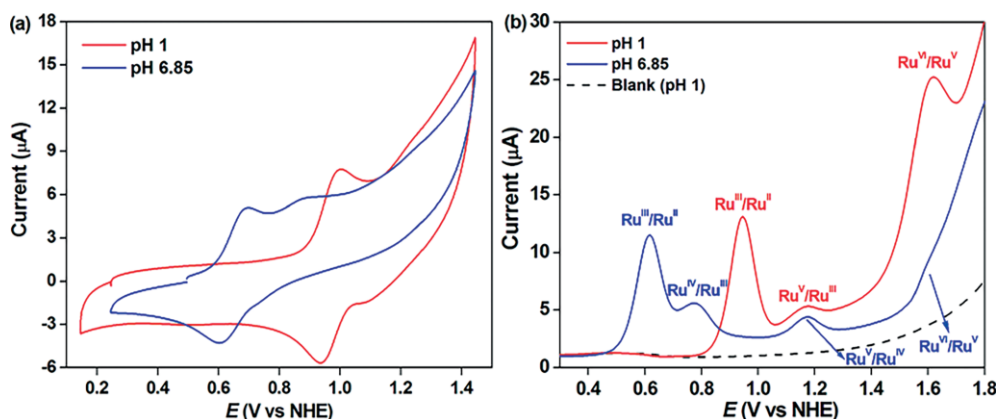


Figure 6. Electrochemical behavior of 2^{Aq} . (a) Cyclic voltammogram (red line) in acidic aqueous solution (pH 1, CF_3SO_3H) and (blue line) in B.-R. buffer at pH 6.85. (b) Square wave voltammogram in (red) acidic aqueous solution (pH 1, CF_3SO_3H); (blue) B.-R. buffer pH 6.85; (black dash) blank at pH 1. Conditions: $[2^{Aq}] = 0.5$ mM, scan rate of CV = 0.1 V s^{-1} , for SWV frequency = 15 Hz, amplitude = 0.025 V, working electrode: glassy carbon.

while the formation of $[\text{Ru}^{\text{IV}}=\text{O}]^{2+}$ is favored in higher pH domain. The next oxidation process is unique in the sense that it involves variable number of electron transfer depending on pH. The oxidation potential remains pH independent in the whole region from pH 1.30 to 11.52, corresponding to formation of $[\text{Ru}^{\text{V}}=\text{O}]^{3+}$ species by $1e^-$ transfer from $[\text{Ru}^{\text{IV}}=\text{O}]^{2+}$ species. In contrast, in pH domain of 0.48–1.30 the oxidation potential decreases linearly with a slope of -60 mV/pH. This phenomenon can be attributed as oxidation from $[\text{Ru}^{\text{III}}-\text{OH}_2]^{3+}$ into $[\text{Ru}^{\text{V}}=\text{O}]^{3+}$, a $(2e^-, 2H^+)$ PCET process which is apparently equivalent to $(1e^-, 1H^+)$ process. As seen in Figure 6b, the intensity of oxidation waves from III \rightarrow IV \rightarrow V in SWV curves are lower than II \rightarrow III wave; this can be argued due to slow heterogeneous electron-transfer kinetics from the solution to the electrode surface as observed commonly for ruthenium-aqua complexes.^[19,22a,24,25] The redox composition of missing $\text{Ru}^{\text{IV}}/\text{Ru}^{\text{III}}$ couple at stronger acidic region now can be attributed by drawing an imaginary line as shown in Figure 7 with a slope of -116 mV/pH which refers to $(1e^-, 2H^+)$ process for $[\text{Ru}^{\text{IV}}=\text{O}]^{2+}/[\text{Ru}^{\text{III}}-\text{OH}_2]^{3+}$ couple. Further oxidation of $[\text{Ru}^{\text{V}}=\text{O}]^{3+}$ species occurs at a relatively constant potential of 1.60 V vs. NHE over the entire pH 0.48–11.52 range. This can be regarded as only electron transfer associated with generation of formal $[\text{Ru}^{\text{VI}}=\text{O}]^{4+}$ species. It is worth noticing that the $[\text{Ru}^{\text{VI}}=\text{O}]^{4+}/[\text{Ru}^{\text{V}}=\text{O}]^{3+}$ couple for **2^{Aq}** lies well above than the thermodynamic potential for the oxidation of water to dioxygen, indicating $[\text{Ru}^{\text{VI}}=\text{O}]^{4+}$ species could potentially trigger the oxidation of water. We have reinvestigated the Pourbaix diagram of **1^{Aq}** at pH 0.50–4.7 (Figures S26–S27) and it differs from that reported by Kojima et al.^[15] The redox compositions of **1^{Aq}** are very similar to those of **2^{Aq}** given the similar coordination environment provided by N_4Py and $\text{N}_2\text{Py-MeBpy-Bz}$ ligand. The pK_a value of $[\text{Ru}^{\text{III}}(\text{N}_4\text{Py})(\text{OH}_2)]^{3+}$ determined from Pourbaix diagram is 2.30, which is higher than that of $[\text{Ru}^{\text{III}}(\text{N}_2\text{Py-MeBpy-Bz})(\text{OH}_2)]^{3+}$ (Table 3). This confirms again $\text{N}_2\text{Py-MeBpy-Bz}$ ligand induces greater Lewis acid character in Ru center than N_4Py .

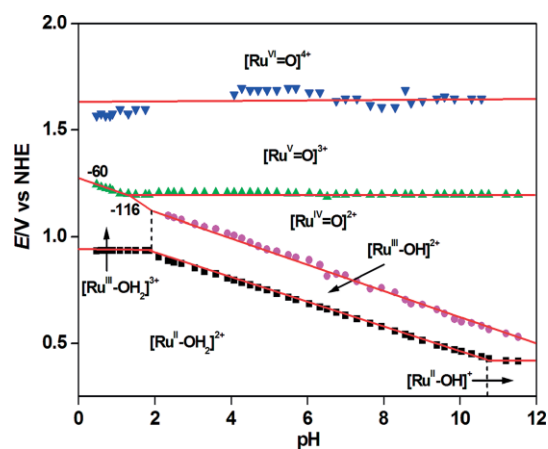


Figure 7. Pourbaix diagram for complex **2^{Aq}**.

Spectroscopic Redox Titration of **2^{Aq}**

The redox titration of complex **2^{Aq}** with ceric ammonium nitrate (CAN) in acid medium (pH 1 aqueous $\text{CF}_3\text{SO}_3\text{H}$ solution) was

performed by UV/Vis spectroscopy to detect intermediates formed upon oxidation. The UV/Vis spectra of **2^{Aq}** at different oxidation states are displayed in Figure 8. The oxidation of Ru^{II} to Ru^{III} complex proceeds in one step, as evident from the three isosbestic points at $\lambda = 332, 308, 281$ nm and the linear increase of 325 nm absorbance band up to the addition of one equivalent of CAN (Figure S28). Upon one electron oxidation the MLCT (467 nm, $\epsilon = 7170 \text{ M}^{-1} \text{ cm}^{-1}$) and $\pi-\pi^*$ (297 nm, $\epsilon = 21525 \text{ M}^{-1} \text{ cm}^{-1}$) bands of **2^{Aq}** are vanished and new bands at 310 nm ($16550 \text{ M}^{-1} \text{ cm}^{-1}$), 322 nm ($15000 \text{ M}^{-1} \text{ cm}^{-1}$) along with a broad band at 365 nm ($4500 \text{ M}^{-1} \text{ cm}^{-1}$) are emerged (Figure S28a), as expected for the formation of Ru^{III} species.^[11f,17a] The formation of Ru^{III} species was further proved by EPR spectroscopy (Figure S29). The EPR spectrum, measured at 77 K, shows a characteristic rhombic signal with $g_x = 2.76, g_y = 2.18, g_z = 1.57$, which is typical for a low-spin $S = 1/2$ Ru^{III} system.^[26] Addition of two more equivalents of CAN to Ru^{III} resulted in bleaching of 365 nm band with lowering the intensity of 310 nm peak ($15200 \text{ M}^{-1} \text{ cm}^{-1}$) (Figure S28b), corresponding to the formation of Ru^{V} species, as evident from isosbestic point at 270 nm (Figure S28b) and the titration curve (Figure S28c). No appreciable spectral changes are observed beyond the addition of third equivalent of CAN, probably due to its rapid consumption for water oxidation catalysis. These finding corroborates well with the electrochemical behaviour of **2^{Aq}** stated before. Therefore, based on the Pourbaix diagram, the course of reactions during titration at pH 1 can be summarized as follows [Equation (1), Equation (2)]:

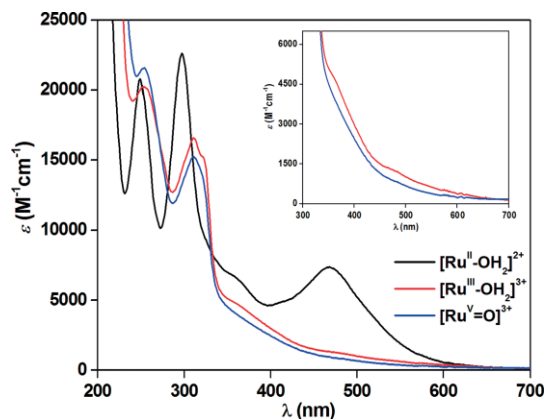
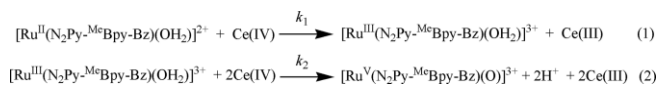


Figure 8. UV/Vis spectra of **2^{Aq}** at different oxidation states: $[\text{Ru}^{\text{II}}-\text{OH}_2]^{2+}$ (black), $[\text{Ru}^{\text{III}}-\text{OH}_2]^{3+}$ (red), and $[\text{Ru}^{\text{V}}=\text{O}]^{3+}$ (blue) generated from stoichiometric oxidation with Ce^{IV} in 0.1 M $\text{CF}_3\text{SO}_3\text{H}$ (pH 1).

Water Oxidation Catalysis

The oxidation of water catalysed by complexes **1^{Aq}** and **2^{Aq}** was investigated using CAN as the oxidant in aqueous $\text{CF}_3\text{SO}_3\text{H}$ solution (initial pH 1). Addition of excess amount of CAN to the degassed solutions of complexes (final conc. of CAN = 60 mM and complex = 1 mM) resulted in rapid O_2 gas evolution. The

evolution of oxygen gas was monitored by Ocean Optic fluorescence-based oxygen sensor (Neofox, FOSPOR-R) positioned in the headspace of the custom made reaction vessel kept at 30 °C using thermostat. The oxygen evolution curves by complexes **1^{Aq}** and **2^{Aq}** are displayed in Figure 9. After ≈ 1.25 h, maximum turn-over numbers (TONs) of ≈ 1 and 6 with conversion efficiency of 6 % and 40 % were obtained for complexes **1^{Aq}** and **2^{Aq}**, respectively.^[27] No oxygen gas was detected without any catalyst, affirming no air leakage occurred during the experiment.

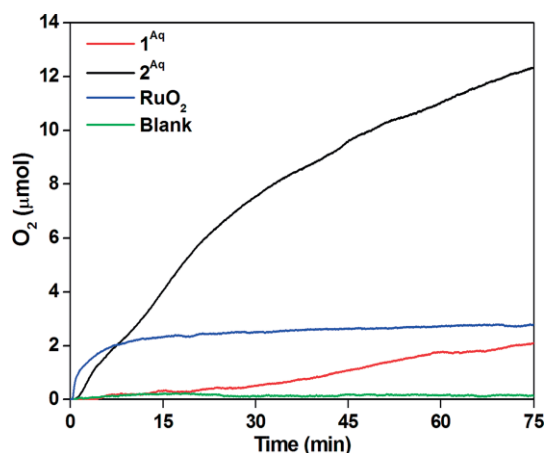


Figure 9. Ce^{IV} driven water oxidation with complex **1^{Aq}** (red line), **2^{Aq}** (black line), RuO₂ (Sigma–Aldrich, CAS: 12036–10–1; blue line) in pH 1 aqueous CF₃SO₃H solution. Conditions: [Cat]_f = 1 mM, [CAN]_f = 60 mM, total volume = 2 mL. The green line represents the blank study.

Clearly, complex **2^{Aq}** showed higher activity compared to complex **1^{Aq}**. This result is in accordance with the catalytic current obtained during electrochemical analysis. Therefore, it is evident that presence of bipyridyl moiety significantly improved the water oxidation activity of **2^{Aq}**. The unique π -acceptor property of bipyridyl moiety most likely finely tunes the electrophilic character of the Ru-oxo moiety, which would in turn control the activity. A similar finding was reported by Zhao et al. where the replacement of one of the pyridine group of tris(2-pyridylmethyl)amine (TPA) ligand with bipyridine improves the catalytic activity of [Ru(DPA-Bpy)(H₂O)]²⁺ complex (DPA-Bpy = *N,N*-Bis(2-pyridinylmethyl)-2,2'-bipyridine-6-methanamine).^[17a] The catalytic performance of **2^{Aq}** is comparable to the reported ones with similar structures;^[17] however the activity is much lower than the most efficient mononuclear Ru complex having pentapyridyl ligand scaffold.^[18]

Since CAN is very strong oxidant, potentially it could oxidize the organic ligands and degrade the catalyst rapidly to something else which might be suspected as actual catalyst to make oxygen.^[28] Thus to establish the catalytic importance of **2^{Aq}** we have verified the stability of complex **2^{Aq}** at initial stage of catalysis using NMR spectroscopy by adding ten equivalents of CAN. The ¹H NMR spectrum obtained after treating the reaction mixture with ascorbic acid clearly indicates catalyst **2^{Aq}** maintained its molecular integrity (Figure S30), implying its true catalyst nature for O₂ evolution. Further we have compared the oxygen evolution kinetics of both the catalysts with catalytically

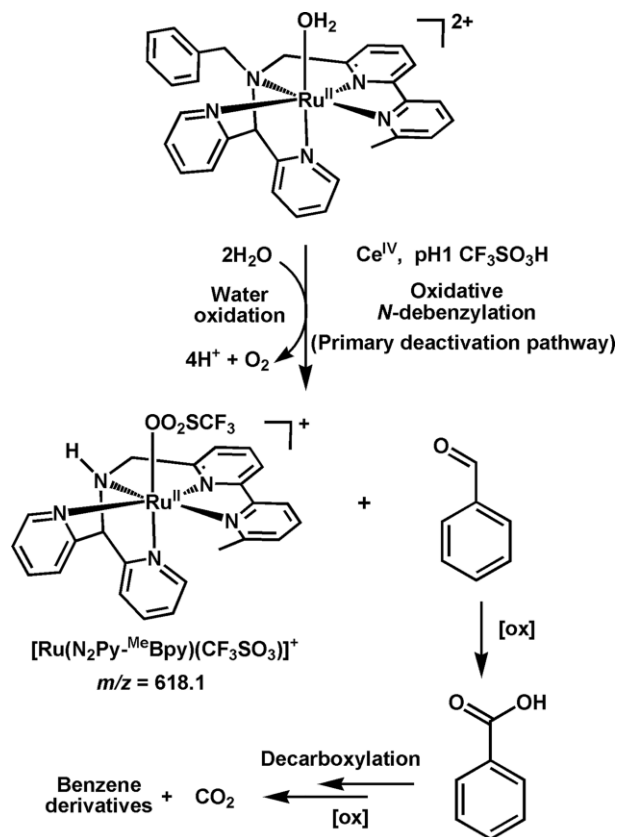
active RuO₂ which might form due to ligand degradation as reported before in literature.^[24] As can be seen from Figure 9, the oxygen evolution kinetics of RuO₂ differs significantly from that of both the catalysts, ruling out the contribution of RuO₂ in water oxidation reaction. Moreover, as seen in Figures S22, S24, the reversible feature of the Ru^{III/II} waves of both the complexes in CV diagram were retained almost fully even if the scan was done upto the electrocatalytic wave at 1.65 V vs. NHE, which can be achieved by CAN at most, implying compounds did not undergo rapid degradation. Although for complex **2^{Aq}** a new wave at 0.7 V was observed probably due to the degraded product (Figure S22 inset). However this degradation does not correlate with the enhanced catalytic activity rather it can be correlated with the deactivation of the catalytic process (see below). These findings strengthen our belief that complexes act as true catalyst rather than a precatalyst.

Deactivation Pathway of Catalyst **2^{Aq}**

Although complex **2^{Aq}** acts as true catalyst and shows moderate activity, oxygen evolution was ceased after a certain time. The major part of CAN remains unconsumed after catalysis, implying other chemical reactions in competition with water oxidation are also occurring with deactivation of water oxidation ability of the catalyst. The potential deactivation pathways for molecular Ru-WOCs would be the denaturation of catalyst due to ligand modification, ligand oxidation or combination of both. Llobet^[29] and other^[17] demonstrated the deactivation of Ru-catalysts via oxidation of methylene groups to CO₂ under oxidizing condition. In order to identify the deactivation pathway for catalyst **2^{Aq}** we performed a catalysis reaction with 1:30 [catalyst]:[CAN] ratio (where ≈ 6 TONs could be achieved) in pH 1 CF₃SO₃H. After completion of the reaction the evolved gas was subjected to GC analysis, showing trace quantity of CO₂ gas formation compared to O₂ (CO₂/O₂ \approx 1:10) (Figure S31). The post-catalysis reaction mixture was then analysed by MALDI mass spectroscopy. A major peak at *m/z* = 618.1 was observed (Figure S32), assigned to [Ru(N₂Py-MeBpy)(CF₃SO₃)]⁺ species where the parent ligand N₂Py-MeBpy-Bz was transformed to N₂Py-MeBpy via oxidative *N*-debenzylation pathway. The *N*-debenzylation process might have propagated via generation of benzyl radical by high valent ruthenium species.^[30] The putative oxidized product of benzyl group such as benzoic acid was detected by GC-MS (Figure S33). The benzoic acid might have been generated via oxidation of benzaldehyde as depicted in Scheme 1. Further addition of another 30 equivalents of CAN into the reaction mixture however did not produce measurable amount of oxygen. Therefore, the product [Ru(N₂Py-MeBpy)(CF₃SO₃)]⁺ could be attributed as deactivated form of the parent catalyst, **2^{Aq}**. These findings indicate that the catalyst underwent denaturation primarily due to the side-reaction where ligand modification took place via oxidative *N*-debenzylation pathway along with minor degradation to CO₂ as shown in Scheme 1.

Kinetic Analysis of Water Oxidation

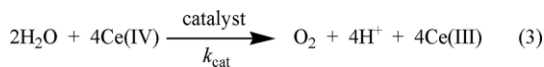
Although the catalytic performance of the complexes is limited to a handful turnovers, the mechanistic study of water oxidation



Scheme 1.

by these mononuclear complexes would be interesting as the water oxidation proceeds via formal ruthenium(VI)-oxo state. To understand the mechanistic steps involved in water oxidation reaction we further performed kinetic study with complexes **1^{Aq}** and **2^{Aq}**. The key step involved in water oxidation catalysis is the O–O bond formation. The following two pathways are well accepted: (i) water nucleophilic attack (WNA) at electron deficient high-valent metal-oxo group, and (ii) bimolecular radical coupling between two metal-oxyl groups (I2M).^[31] To know which pathway O–O bond formation occurred, the kinetic studies were carried out under excess Ce^{IV} condition at pH 1 $\text{CF}_3\text{SO}_3\text{H}$ solution with both the Ru^{II} complexes. The rate of re-

action was followed by monitoring the consumption of Ce^{IV} in presence of catalyst using UV/Vis spectrophotometer. The 360 nm band was chosen to follow the Ce^{IV} consumption (Figures S34–S35 for **2^{Aq}**). The initial rates of Ce^{IV} consumption were used to analyse the kinetic data to avoid the effect of decomposition of catalysts under strongly oxidizing conditions. When the initial concentration of CAN was kept constant (1.5 mM) and that of catalyst concentrations were changed (10–25 μM), the initial rates of Ce^{IV} consumption were found to be linearly dependent to the concentrations of **1^{Aq}** and **2^{Aq}** (Figure S36 for **1^{Aq}** and Figure 10a for **2^{Aq}**), implying first-order dependence of catalyst concentration on rate. The kinetic studies were also performed keeping initial concentration of both the catalysts constant (0.015 mM) with varying concentration of CAN (0.75–3.00 mM). The initial rate of Ce^{IV} consumption by **1^{Aq}** was found to be independent with CAN concentration. On the other hand the initial rate of Ce^{IV} consumption by **2^{Aq}** was partially dependent on $[\text{Ce}^{\text{IV}}]$ (order < 1). An order was estimated to be 0.23 by plotting $\ln(\text{initial rate})$ vs. $\ln[\text{Ce}^{\text{IV}}]$ (Figure 10b).^[25] This implies that there is an auxiliary path consuming Ce^{IV} simultaneously. This auxiliary path might be correlated with the oxidative N-debenzylation process leading to the deactivation of catalytic activity of **2^{Aq}** (Scheme 1). By neglecting the minor path for **2^{Aq}**, formally the rate law for both the complexes can be expressed as $\text{rate} = k_{\text{obs}}[\text{catalyst}]^1$. The k_{obs} values were calculated to be $1.21 \times 10^{-3} \text{ s}^{-1}$ and $4.00 \times 10^{-2} \text{ s}^{-1}$ at 30 °C for **1^{Aq}** and **2^{Aq}**, respectively. Thus the $k_{\text{cat}} = 3.03 \times 10^{-4} \text{ s}^{-1}$ for **1^{Aq}** and $k_{\text{cat}} = 1.00 \times 10^{-2} \text{ s}^{-1}$ for **2^{Aq}** of the overall catalytic water oxidation [Equation (3)] can be calculated as one-fourth of k_{obs} since four equivalents of Ce^{IV} were consumed for generation of one equivalent of dioxygen.



The first-order dependence of rate with respect to catalyst concentration implies a mononuclear mechanism where O–O bond formation takes place via water nucleophilic attack (WNA) on formal high-valent $[\text{Ru}^{\text{VI}}=\text{O}]^{4+}$ species. The difference in reactivity towards water oxidation for complexes **1^{Aq}** and **2^{Aq}** could be rationalized by considering higher Lewis acid character of metal center in **2^{Aq}** than **1^{Aq}**, as evident from $\text{p}K_{\text{a}}$ values, which

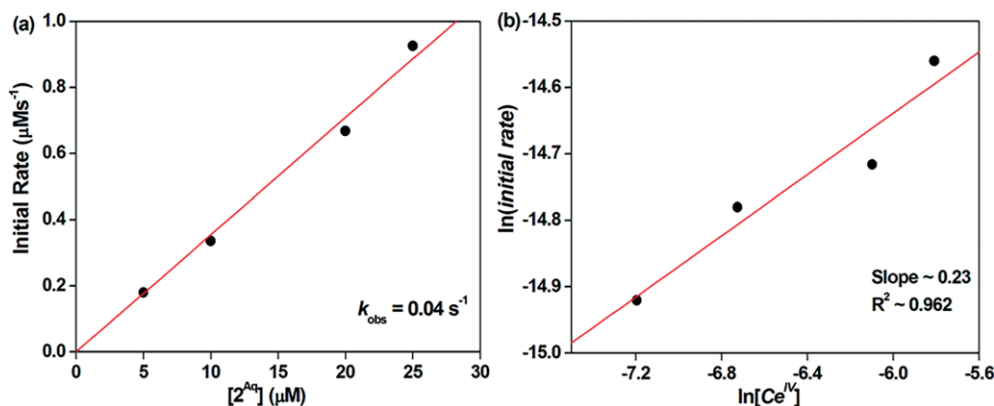
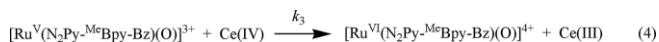


Figure 10. (a) Plot of initial rate of Ce^{IV} consumption vs. $[\mathbf{2}^{\text{Aq}}]$ at 1.5 mM CAN; (b) Plot of $\ln(\text{initial rate})$ of Ce^{IV} consumption vs. $\ln[\text{Ce}^{\text{IV}}]$ in the presence of **2^{Aq}**.

might induce greater electrophilic character in Ru–O bond for **2^{Aq}**, facilitating the water nucleophilic attack. An expansion of coordination number from six to seven at high-valent state of **1^{Aq}**, as demonstrated by Kojima et al.,^[15] might also be taken into account in rendering the electrophilicity of Ru–O bond.

As **2^{Aq}** shows much higher activity than **1^{Aq}** we further focus our kinetic study with **2^{Aq}** to get deeper insights of the mechanistic steps. The oxidations of Ru^{II} → Ru^{III} and Ru^{III} → Ru^V [Equation (1) & (2), respectively] with CAN at pH 1 occurred very rapidly and we could not determine the rates k_1 and k_2 , respectively, due to lack of stopped-flow techniques. Nevertheless these two oxidation steps are expected to occur very fast since the redox potential of Ce^{IV}/Ce^{III} couple at pH 1 (1.61 V vs. NHE) is high enough to proceed the first and second oxidation processes at the diffusion-limited rate. So it could be presumed that k_1 and k_2 values would be much higher than catalytic rate k_{cat} [Equation (3)] and none of these electron transfer events would represent the rate-determining step of the catalytic cycle. Upon addition of another one equivalent of CAN to the resulting [Ru^V=O]³⁺ species, a Ru^V → Ru^{VI} electron-transfer step [Equation (4)] followed by water nucleophilic attack at formally [Ru^{VI}=O]⁴⁺ species to generate putative [Ru^{IV}-OOH]³⁺ species [Equation (5)] can be rationalized by biphasic time-resolved absorbance trace (Figure 11).

The global analysis (performed with ReactLab Kinetics version 1.1),^[32] based on the model in Equation (4) and (5) afforded the rate constants as $k_3 = 2.90 \times 10^2 \text{ M}^{-1}\text{s}^{-1}$, $k_{O-O} = 1.27 \times 10^{-2} \text{ s}^{-1}$. The experimental spectral changes, the fitted time trace at



360 nm, calculated spectra for the various species involved during catalysis [Ru^V=O]³⁺, [Ru^{VI}=O]⁴⁺, [Ru^{IV}-OOH]³⁺ and the calculated diagram for their time-dependent distributions are displayed in Figure 11. The calculated absorption profiles of [Ru^V=O]³⁺, [Ru^{VI}=O]⁴⁺ and [Ru^{IV}-OOH]³⁺ (Figure 11c) are in accordance with the observed spectral profiles at $t = 0, 40$ and 250 s (Figure 11a), when the corresponding species are estimated to be predominant according to the calculated species distribution diagram (Figure 11d). The rate constant values for the reactions involved in the catalytic reaction are summarized in Table 4. The rate constant for O–O bond formation (k_{O-O}) is little higher but comparable with regard to the catalytic rate constant, k_{cat} . Therefore it can be concluded that the O–O bond formation [Equation (5)] to generate the [Ru^{IV}-OOH]³⁺ species is likely to be the rate-determining step for water oxidation catalysed by **2^{Aq}**. The calculated structure of [Ru^{IV}-OOH]³⁺ species (Figure S37a, Table S3) by DFT method and the obtained O–O bond length (1.378 Å) is in accordance with the characteristic metal-peroxo complex. The subsequent step prior to oxygen liberation might include proton-coupled oxidation of [Ru^{IV}-OOH]³⁺ to [Ru^V-OO]³⁺ species, as proposed in previous studies.^[19,23a,23c] This step should not be a rate-determining step since the overall catalytic reaction is zero-order with respect to CAN concentration. The final step would follow the liberation of oxygen

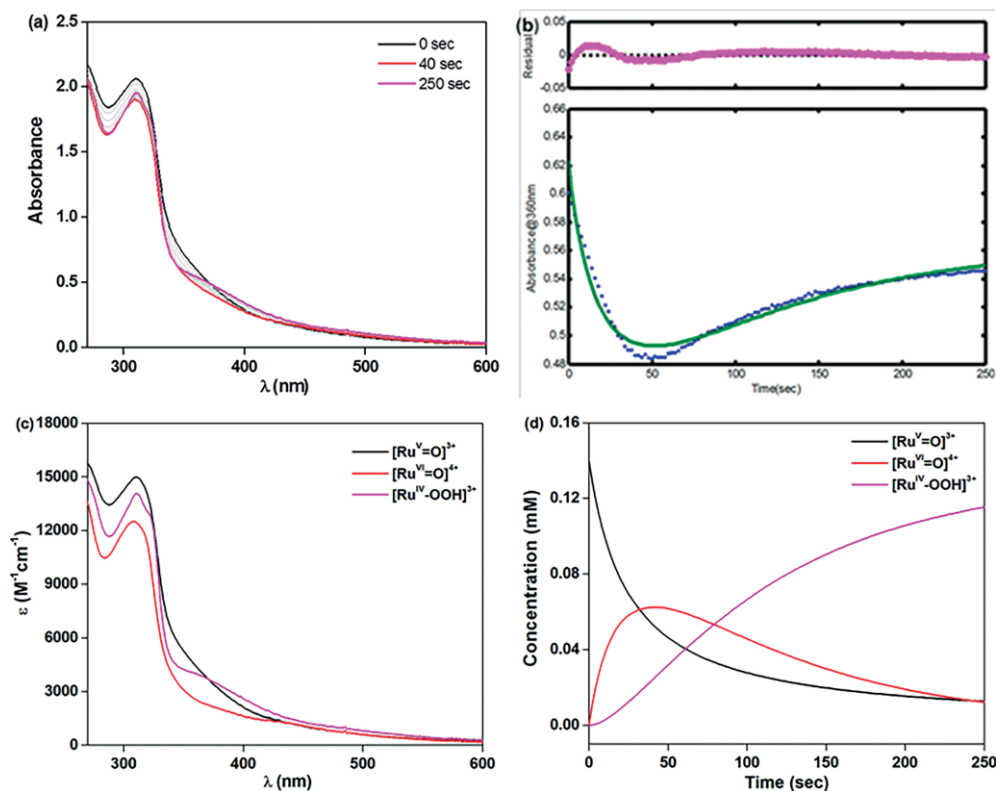


Figure 11. Kinetics and spectroscopic data for formation of [Ru^{VI}=O]⁴⁺ from [Ru^V=O]³⁺ and subsequent formation of [Ru^{IV}-OOH]³⁺. (a) Spectral changes after addition of one equivalent of CAN to [Ru^V=O]³⁺ in pH 1 CF₃SO₃H, [2^{Aq}] = 0.14 mM. (b) Absorption trace at 360 nm (experimental points: blue dots; fitting: green line). (c) Calculated absorption spectra of Ru-species based on global analysis. (d) Species distribution diagram vs. time.

from $[\text{Ru}^{\text{V}}\text{-OO}]^{3+}$ via reductive elimination pathway. This step is believed to be rapid as was demonstrated before by Meyer and co-workers with $[\text{Ru}(\text{tpy})(\text{bpm})(\text{OH}_2)]^{2+}$ ($\text{tpy} = 2,2':6',2''\text{-terpyridine}$; $\text{bpm} = 2,2'\text{-bipyrimidine}$) complex at pH 0/ Ce^{IV} condition.^[19b] The optimized six-coordinate structure with terminal peroxide of $[\text{Ru}^{\text{V}}\text{-OO}]^{3+}$ is shown in Figure S37b (Table S4). The structure is antiferromagnetically coupled doublet, as determined by Mulliken atomic spin densities (Ru , -0.77 ; $\text{O}_{(\text{proximal})}$, 0.84 ; $\text{O}_{(\text{distal})}$, 1.06 , Figure S37c). The O–O bond length obtained is 1.21 \AA , implying it can be described as a $d^5 \text{ Ru}^{\text{III}}$ complex coordinated to triplet oxygen.

Table 4. Summary of rate constants of Ce^{IV} driven water oxidation catalysed by 2^{Aq} in pH 1 $\text{CF}_3\text{SO}_3\text{H}$ at $30 \text{ }^\circ\text{C}$.

Reaction description	Rate constant	
Equation (1)	k_1	Rapid
Equation (2)	k_2	Rapid
Equation (4) ^[a]	k_3	$2.90 \times 10^2 \text{ M}^{-1} \text{ s}^{-1}$
Equation (5) ^[a]	$k_{\text{O-O}}$	$1.27 \times 10^{-2} \text{ s}^{-1}$
Equation (3) ^[b]	k_{cat}	$1.00 \times 10^{-2} \text{ s}^{-1}$

[a] Calculated from global analysis. [b] Determined spectrophotometrically under excess Ce^{IV} condition.

Therefore, on the basis of the discussions stated above we proposed a catalytic cycle of water oxidation by 2^{Aq} at pH 1 as shown in Figure 12.

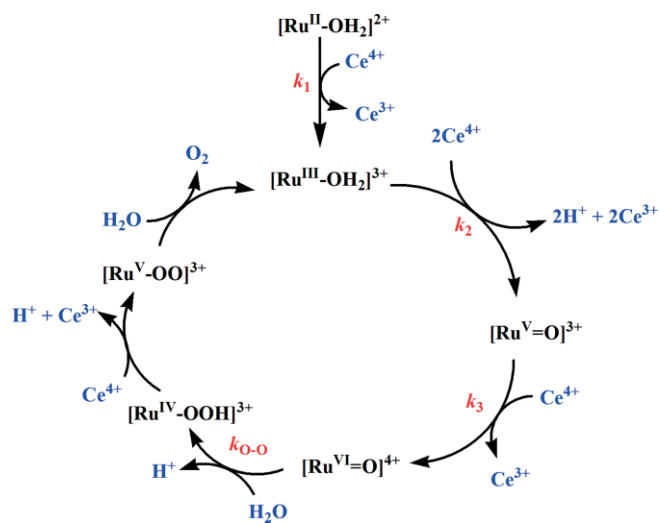


Figure 12. Proposed mechanism for water oxidation by 2^{Aq} at pH 1.

Conclusions

In this paper, we report the syntheses and characterizations of new mononuclear Ru^{II} complexes with a newly designed pentadentate ligand, $\text{N}_2\text{Py-MeBpy-Bz}$. Using Ce^{IV} as oxidant, the Ru-aqua complex, 2^{Aq} catalyzed the oxidation of water more efficiently than analogous complex 1^{Aq} . The presence of bipyridyl moiety in the ligand architecture of complex 2^{Aq} significantly improves the catalytic activity; thus the performance of a catalyst highly depends on the electronic perturbation exerted by

the ligand scaffold. Electrochemical studies along with kinetic analysis on complex 2^{Aq} suggest a mechanism where a formal $[\text{Ru}^{\text{VI}}=\text{O}]^{4+}$ species acts as an active intermediate which triggers the O–O bond formation via water nucleophilic attack in a rate-limiting step. The strong σ -donating property of the pentadentate scaffold helps to access such a high oxidation state. The deactivation study on 2^{Aq} revealed that the benzyl group is prone to undergo oxidation under oxidizing condition. The oxidative *N*-debenzylation process leads to the deactivation of catalyst. The deactivated Ru complex and the oxidized product of benzyl group such as benzoic acid were detected by mass spectroscopy and GC–MS, respectively. Therefore the present study revealed a new reaction mechanism for activation of water molecule as well as the deactivation pathway that might provide a lesson for the future development of efficient WOCs.

Experimental Section

Reagents and Materials: All reagents used in the present work were obtained from commercial sources (Sigma Aldrich, Alfa Aesar, TCI Chemicals (India) Pvt. Ltd. and Sisco Research Laboratories Pvt. Ltd. (SRL) India) and were used without further purification. All organic solvents were purified/dried prior to use. Milli-Q water ($18.2 \text{ M}\Omega$) was used in preparation of pH 1 solution with trifluoromethanesulfonic acid ($\text{CF}_3\text{SO}_3\text{H}$). Di-2-pyridylmethanamine,^[20a] 6'-methyl-2,2'-bipyridine-6-carbaldehyde^[20b] and *cis*- $[\text{Ru}(\text{DMSO})_4\text{-Cl}_2]$,^[20c] were prepared according to the literature method.

Syntheses of Ligands

***N,N*-Bis(2-pyridylmethyl)-*N*-(bis-2-pyridylmethyl)amine (N_4Py):** It was synthesized from di-2-pyridylmethanamine and 2-picoyl chloride hydrochloride under basic condition as described previously.^[15]

***N*-Benzyl-*N*-((6-(6-methylpyridin-2-yl)pyridin-2-yl)methyl)dipyridin-2-yl-methanamine ($\text{N}_2\text{Py-MeBpy-Bz}$):** The synthetic strategy comprises the following two steps.

Step 1: Synthesis of *N*-((6-(6-Methylpyridin-2-yl)pyridin-2-yl)methyl)dipyridin-2-yl-methanamine ($\text{N}_2\text{Py-MeBpy}$): Di-2-pyridylmethanamine (0.234 g , 1.261 mmol) and 6'-methyl-2,2'-bipyridine-6-carbaldehyde (0.250 g , 1.261 mmol) were taken together in 100 mL round-bottom flask and dissolved in methanol (20 mL). After stirring the reaction mixture for about 24 hours, an off-white solid residue was isolated. The solid was then dissolved in 3:1 methanol-chloroform mixture and NaBH_4 (0.120 g , 3.172 mmol) was added portionwise to it at $0 \text{ }^\circ\text{C}$. The resulting solution was stirred overnight at room temperature and then the solvent was evaporated. The residue was treated with brine solution and extracted with $3 \times 50 \text{ mL}$ of CH_2Cl_2 . The combined organic layers were dried with anhydrous Na_2SO_4 , filtered and concentrated under reduced pressure to afford the desired product as pale yellow oil (0.400 g , Yield 86%). $^1\text{H NMR}$ (400 MHz , 300K , CDCl_3): δ (ppm) = 2.63 (s, 3 H), 4.02 (s, 2 H), 5.24 (s, 1 H), 7.15 (m, 3 H), 7.34 (d, 1 H), 7.51 (m, 2 H), 7.61 – 7.70 (m, 3 H), 7.74 (t, 1 H), 8.21 (d, 1 H), 8.27 (d, 1 H), 8.59 (d, 2 H).

Step 2: Synthesis of *N*-Benzyl-*N*-((6-(6-methylpyridin-2-yl)pyridin-2-yl)methyl)dipyridin-2-yl-methanamine ($\text{N}_2\text{Py-MeBpy-Bz}$): A mixture of benzyl chloride (0.133 g , 1.051 mmol), $\text{N}_2\text{Py-MeBpy}$ (0.386 g , 1.050 mmol) and catalytic amount of KI (0.100 g , 0.602 mmol) in MeCN (50 mL) was stirred under dinitrogen atmosphere. To the reaction mixture a solution of diisopropylethylamine

(DIPEA) (1.362 g, 10.539 mmol) in MeCN (20 mL) was added dropwise over a period of 30 minutes and it was heated to reflux for 48 hours under dinitrogen atmosphere. After cooling to room temperature the resulting mixture was filtered through Celite and then the solvent was evaporated under reduced pressure. The residue was dissolved in dichloromethane (30 mL) and was washed with water (3 × 30 mL). The organic layer was dried with anhydrous MgSO₄. Evaporation of the solvent yielded the crude product as yellow oil. Purification was achieved by column chromatography on silica using hexane, ethyl acetate, methanol (2:2:1) mixture to afford 0.425 g of ligand (Yield 88 %). ¹H NMR (400 MHz, 300K, CDCl₃): δ (ppm) = 2.62 (s, 3 H), 3.84 (s, 2 H), 3.96 (s, 2H), 5.39 (s, 1 H), 7.13–7.26 (m, 7H), 7.46 (t, 3H), 7.65–7.75 (m, 5H), 8.22 (t, 2H), 8.57 (d, 2H). ¹³C NMR (150 MHz, 300K, CDCl₃): δ (ppm) = 27.64 (CH₃), 39.95 (PhCH₂NCH₂bpy), 47.59 (Py₂CHN), 114.08, 125.27, 125.66, 126.42, 126.99, 127.67, 127.75, 128.12, 128.24, 136.85, 139.28, 146.09, 146.44, 147.97, 149.18.

Syntheses of Mononuclear Ru^{II} Complexes

[Ru(N₄Py)(Cl)](PF₆) (1^{Cl}): It was synthesized by literature procedure.^[15] N₄Py (0.400 g, 1.089 mmol) and *cis*-[Ru(DMSO)₄Cl₂] (0.528 g, 1.089 mmol) were taken together in a two-necked round-bottomed flask. Approximately 60 mL of 2-propanol was added and the solution was refluxed for 12 h under dinitrogen atmosphere. The reaction mixture was then cooled to room temperature and removal of the solvent under reduced pressure resulted dark brown residue. The residue was then dissolved in ≈ 3 mL of water. Upon addition of saturated aqueous solution of NH₄PF₆ (1 mL), reddish-brown solid emerged. The precipitate was then collected by filtration. The crude product was purified by column chromatography on silica using CHCl₃/MeOH (9:1 v/v) mixture of solvent as eluent. After removal of the solvent a reddish-orange solid was obtained. It was then washed with diethyl ether and then dried in vacuo. Yield: 0.210 g (30 %). Single crystals suitable for X-ray structure determination were obtained by slow evaporation of methanol solution of the complex. Anal. Calc. (%) for [Ru(N₄Py)(Cl)](PF₆)₂ (C₂₃H₂₁ClF₆N₅PRu): C 42.57, H 3.26, N 10.79; found C 42.48, H 3.20, N 10.54. IR [solid sample in KBr (cm⁻¹), selected peaks]: 842 (ν(PF₆⁻)). MALDI (2,5-dihydroxybenzoic acid, dhb as matrix, in methanol): *m/z* = 504.1 [[Ru(N₄Py)(Cl)](PF₆) - PF₆⁻]⁺; 622.3 [[Ru(N₄Py)(Cl)](PF₆) + dhb - H⁺ - Cl⁻ - PF₆⁻]⁺. ¹H NMR (400 MHz, 300K, CD₃CN): δ (ppm) = 4.24 and 4.35 (AB_q, 4 H, J_{AB} = 17.6 Hz, NCH₂Py), 6.38 (s, 1 H, NCHPy₂), 7.01 (d, 2 H, J = 7.6 Hz, H3 of Py₂CHN), 7.26 (t, 2 H, H5 of Py₂CHN), 7.33 (t, 2 H, H5 of PyCH₂N), 7.55–7.60 (m, 2 H, H4 of Py₂CHN), 7.82–7.89 (m, 4 H, H3 of PyCH₂N and H4 of PyCH₂N), 9.00 (d, 2 H, J = 4 Hz, H6 of PyCH₂N), 9.37 (d, 2 H, J = 4 Hz, H6 of Py₂CHN). ¹³C NMR (100 MHz, 300K, CD₃CN): δ (ppm) = 64.67 (NCH₂Py), 78.50 (Py₂CHN), 120.53, 123.85, 124.15, 124.69, 136.08, 136.57, 152.54, 155.26, 160.72, 163.97. Electronic spectrum [λ_{max}, nm (ε, M⁻¹ cm⁻¹)] (in MeCN): 470 (11300), 382 (13600), 300 sh (3600), 257 (10740).

[Ru(N₄Py)(OH₂)](PF₆)₂ (1^{Aq}): This complex was prepared by slight modification of the reported procedure.^[15] A solution of 1^{Cl} (0.200 g, 0.308 mmol) and AgPF₆ (0.778 g, 3.075 mmol) in 80 mL of water was refluxed for 12 h. The reaction mixture was then cooled to ice bath. The insoluble white solid was removed by filtration through Celite pad. The filtrate was concentrated to ≈ 8 mL and addition of 1–2 drops of saturated aqueous solution of NH₄PF₆ resulted the formation of yellow precipitate. The yellow precipitate was recrystallized from warmed water. Yield: 0.120 g (50 %). Anal. calcd. (%) for [Ru(N₄Py)(OH₂)](PF₆)₂ (C₂₃H₂₃N₅ORuP₂F₁₂): C 35.58, H 2.99, N 9.02; found C 35.48, H 2.80, N 8.95. IR [solid sample in KBr (cm⁻¹), selected peaks]: 843 (ν(PF₆⁻)); 3410 (ν(OH) of water). MALDI (2,5-dihydroxybenzoic acid, dhb as matrix, in 0.1 M aqueous

CF₃SO₃H solution): *m/z* = 618.1 [[Ru(N₄Py)(OH₂)](PF₆)₂ - H₂O - 2PF₆⁻ + CF₃SO₃⁻]⁺. ¹H NMR (D₂O): δ (ppm) = 4.24 and 4.37 (AB_q, 4 H, J_{AB} = 17.4 Hz, NCH₂Py), 6.38 (s, 1 H, NCHPy₂), 6.98 (d, 2 H, J = 8 Hz, H3 of Py₂CHN), 7.22 (m, 2 H, H5 of Py₂CHN), 7.31 (m, 2 H, H5 of PyCH₂N), 7.53 (t, 2 H, H4 of Py₂CHN), 7.85 (m, 4 H, H3 of PyCH₂N and H4 of PyCH₂N), 8.77 (d, 2 H, J = 5.2 Hz, H6 of PyCH₂N), 8.86 (d, 2 H, J = 5.2 Hz, H6 of Py₂CHN). Electronic spectrum [λ_{max}, nm (ε, M⁻¹ cm⁻¹)] (in 0.1 M aqueous CF₃SO₃H solution): 440 (6000), 360 (7670), 246 (12000).

[Ru(N₂Py-MeBpy-Bz)(Cl)](PF₆)-MeCN (2^{Cl}-MeCN): To a refluxed solution of *cis*-[Ru(DMSO)₄Cl₂] (0.631 g, 1.302 mmol) and anhydrous LiCl (0.552 g, 13.020 mmol) in MeOH (60 mL) was added dropwise a methanolic solution (10 mL) of N₂Py-MeBpy-Bz (0.596 g, 1.302 mmol) over a period of 30 minutes. The reaction mixture was then refluxed for 12 hours under dinitrogen atmosphere. The crude reaction mixture was then filtered to remove inorganic particles. The filtrate was concentrated in reduced pressure and cooled to 8 °C. Addition of saturated aqueous solution of NH₄PF₆ (1 mL) afforded reddish-brown precipitate. The solid was collected by filtration, washed with cold water and diethyl ether, and dried in vacuo. The product was purified by column chromatography on silica using dichloromethane/methanol (20:1) mixture as an eluent. Removal of solvent afforded the product as dark brown solid. It was then recrystallized by slow diffusion of diethyl ether into a concentrated solution of complex in MeCN. Single crystals suitable for X-ray crystallography were also obtained by this method. Yield: 0.325 g, ≈ 32 %. Anal. Calc. (%) for [Ru(N₂Py-MeBpy-Bz)(Cl)](PF₆)-MeCN (C₃₂H₃₀ClF₆N₆PRu): C, 49.27; H, 3.88; N, 10.77; found C, 49.32; H, 3.75; N, 10.70. IR [solid sample in KBr (cm⁻¹), selected peaks]: 841 (ν(PF₆⁻)). MALDI (2,5-dihydroxybenzoic acid, dhb as matrix, in MeCN): *m/z* 594.1 [[Ru(N₂Py-MeBpy-Bz)(Cl)](PF₆) - (PF₆⁻)]⁺. ¹H NMR (400 MHz, 300K, CD₃CN): δ (ppm) = 2.80 (s, 3 H, bpyCH₃), 3.27 (d, 1 H, J_{ab} = 15.2 Hz, -NCH^aH^bPh), 3.74 (d, 1 H, J_{cd} = 17.6 Hz, -NCH^cH^dbpy), 4.16 (d, 1 H, J_{ab} = 15.2 Hz, -NCH^aH^bPh), 4.52 (d, 1 H, J_{cd} = 17.6 Hz, -NCH^cH^dbpy), 6.06 (s, 1 H, Py₂CHN), 7.01 (t, 1 H, J = 4 Hz), 7.27 (d, 1 H, J = 8 Hz), 7.35 (m, 2 H), 7.51 (m, 3 H), 7.62 (d, 2 H, J = 8 Hz), 7.70–7.81 (m, 4 H), 7.94 (t, 1 H, J = 8 Hz), 8.04–8.12 (m, 2 H), 8.17–8.23 (m, 2 H), 9.60 (d, 1 H, J = 5.2 Hz, H6 of Py^{ax}Py^{eq}CHN). ¹³C NMR (100 MHz, 300K, CD₃CN): δ (ppm) = 26.92 (bpyCH₃), 58.38 (-NCH₂Ph), 60.92 (-NCH₂bpy), 74.73 (Py₂CHN), 120.24, 120.42, 121.90, 123.60, 125.02, 125.66, 126.74, 127.79, 129.23, 131.75, 132.02, 134.30, 135.11, 135.96, 136.63, 138.06, 149.15, 155.21, 157.98, 159.01, 159.63, 160.26, 162.58, 164.90. (Electronic spectrum [λ_{max}, nm (ε, M⁻¹ cm⁻¹)] (in MeCN): 509 (8335), 435 (5240), 353 (7640), 340 (7640), 302 (23730), 251 (21780).

[Ru(N₂Py-MeBpy-Bz)(OH₂)](PF₆)₂·3H₂O-MeOH (2^{Aq}·3H₂O-MeOH): To a solution of 2^{Cl} (0.150 g, 0.202 mmol) in 20 mL of methanol/water mixture (1:1) was added dropwise an aqueous solution of AgPF₆ (0.204 g, 0.808 mmol) under dinitrogen atmosphere. The reaction mixture was refluxed overnight, and the white precipitate was separated by filtration through Celite pad. The filtrate was collected and solvent was removed under reduced pressure until precipitation appeared. It was then collected and washed with diethyl ether and dried in vacuo to yield a reddish-brown solid. Yield: 0.100 g, ≈ 52 %. Anal. Calc. (%) for [Ru(N₂Py-MeBpy-Bz)(OH₂)](PF₆)₂·3H₂O-MeOH (C₃₁H₃₉F₁₂N₅O₅P₂Ru): C, 39.08; H, 4.13; N, 7.35; found C, 39.04; H, 4.07; N, 7.38. IR [solid sample in KBr (cm⁻¹), selected peaks]: 3450 (ν(OH) of water), 840 (ν(PF₆⁻)). MALDI (2,5-dihydroxybenzoic acid, dhb as matrix, in 0.1 M aqueous CF₃SO₃H solution): *m/z* = 708.1 [[Ru(N₂Py-MeBpy-Bz)(OH₂)](PF₆)₂ - H₂O - 2PF₆⁻ + CF₃SO₃⁻]⁺. ¹H NMR (400 MHz, 300K, D₂O): δ (ppm) = 2.79 (s, 3 H, bpyCH₃), 3.39 (d, 1 H, J_{ab} = 14.4 Hz, -CH^aH^bPh), 3.78–3.87 (m, 2 H, -CH^aH^bPh & -CH^cH^dbpy), 4.60 (d, 1 H, J_{cd} = 17.6 Hz, -CH^cH^dbpy), 6.09

(s, 1 H, Py_2CHN -), 6.89 (t, 1 H, $J = 4$ Hz), 7.26 (d, 1 H, $J = 4$ Hz), 7.30–7.32 (m, 2 H), 7.46–7.48 (m, 3 H), 7.53–7.63 (m, 4 H), 7.70 (d, 1 H, $J = 4$ Hz), 7.78 (t, 1 H, $J = 4$ Hz), 7.93 (t, 1 H, $J = 4$ Hz), 8.07–8.08 (m, 2 H), 8.18 (d, 1 H, $J = 8$ Hz), 8.22 (d, 1 H, $J = 8$ Hz), 9.50 (d, 1 H, $J = 8$ Hz, H6 of $\text{Py}^{\text{ax}}\text{Py}^{\text{eq}}$ -CH-N). Electronic spectrum [λ_{max} , nm (ϵ , $\text{M}^{-1} \text{cm}^{-1}$)] (in 0.1M aqueous $\text{CF}_3\text{SO}_3\text{H}$ solution): 467 (7170), 360 sh (6020), 297 (21525), 248 (19280).

[Ru(N_2Py - Me^{e} Bpy-Bz)(MeCN)](PF_6) $_2$ ·0.5MeCN·H $_2$ O (2 $^{\text{ACN}}$ ·0.5MeCN·H $_2$ O): This complex was obtained during recrystallization of 2 $^{\text{Aq}}$ by slow diffusion of diethyl ether into a concentrated solution of the complex in acetonitrile. Single crystals suitable for X-ray crystallography were obtained by the same method. It was found that during crystallization process water was replaced by MeCN. Anal Calcd (%) for [Ru(N_2Py - Me^{e} Bpy-Bz)(MeCN)](PF_6) $_2$ ·0.5MeCN·H $_2$ O ($\text{C}_{33}\text{H}_{33.5}\text{F}_{12}\text{N}_{6.5}\text{OP}_2\text{Ru}$): C, 42.70; H, 3.64; N, 9.81; found C, 32.64; H, 3.37; N, 9.88. IR [solid sample in KBr (cm^{-1})], selected peaks: 2250 ($\nu(\text{C}\equiv\text{N})$ of acetonitrile), 840 ($\nu(\text{PF}_6^-)$). ^1H NMR (400 MHz, 300K, CD_3CN): δ (ppm) = 2.83 (s, 3 H, bpyCH_3), 3.45 (d, 1 H, $J_{\text{ab}} = 14.4$ Hz, $-\text{NCH}^{\text{a}}\text{H}^{\text{b}}\text{Ph}$), 3.85 (d, 1 H, $J_{\text{cd}} = 18.0$ Hz, $-\text{NCH}^{\text{c}}\text{H}^{\text{d}}\text{bpy}$), 4.17 (d, 1 H, $J_{\text{ab}} = 14.4$ Hz, $-\text{NCH}^{\text{a}}\text{H}^{\text{b}}\text{Ph}$), 4.76 (d, 1 H, $J_{\text{cd}} = 18.0$ Hz, $-\text{NCH}^{\text{c}}\text{H}^{\text{d}}\text{bpy}$), 6.15 (s, 1 H, Py_2CHN -), 7.14 (t, 1 H, $J = 6$ Hz), 7.39–7.42 (m, 3 H), 7.58 (m, 3 H), 7.68 (t, 1 H, $J = 6$ Hz), 7.74 (d, 1 H, $J = 7.6$ Hz), 7.77–7.80 (m, 2 H), 7.86 (t, 1 H, $J = 8$ Hz), 7.96 (t, 1 H, $J = 8$ Hz), 8.08–8.21 (m, 3 H), 8.28 (t, 2 H, $J = 8$ Hz), 9.51 (d, 1 H, $J = 5.2$ Hz, H6 of $\text{Py}^{\text{ax}}\text{Py}^{\text{eq}}$ CHN). ^{13}C NMR (100 MHz, 300K, CD_3CN): δ (ppm) = 27.03 (bpyCH_3), 59.17 ($-\text{NCH}_2\text{Ph}$), 61.25 ($-\text{NCH}_2\text{bpy}$), 74.34 (Py_2CHN), 121.08, 121.71, 122.33, 124.25, 125.47, 126.29, 126.68, 129.19, 129.82, 130.85, 132.11, 136.65, 138.15, 139.34, 154.32, 157.22, 158.07, 158.50, 158.69, 159.74, 162.84, 165.74. Electronic spectrum [λ_{max} , nm (ϵ , $\text{M}^{-1} \text{cm}^{-1}$)] (in MeCN): 490 sh (3700), 437 (8250), 397 (7200), 291 (22360), 254 (15250).

Physical Measurements

General Instrumentation: Elemental analyses (C, H, N) were obtained using Perkin–Elmer Elemental Analyzer (Model No 2400-SERIESII). Spectroscopic measurements were made using the following instruments: Electronic: Agilent 8454 diode-array spectrophotometer. FTIR (KBr, 4000–500 cm^{-1}): Thermofisher Scientific Nicolet 6700 FTIR. MALDI: Bruker MALDI-TOF/TOF Ultraflexxtreme; X-band EPR: Bruker ELEXSYS 580 spectrometer. NMR spectra were obtained on Bruker 400/600 Ultrashield (400 MHz/600 MHz) NMR spectrometer; chemical shifts are reported in ppm referenced to solvent residual peak. Purification of water (18.2 M Ω cm) was performed with a Milli-Q system (Millipore, Direct-Q 3 UV). pH was measured by Utech pH tutor. O_2 and CO_2 gases were detected by GC (Thermofisher Scientific Trace 1110 GC) with TCD and FID, respectively. GC–MS analysis was carried out on Thermo Scientific Trace 1300 gas chromatograph connected with ISQ single quadrupole MS. The products were identified by comparing their retention times and mass spectral patterns to those authentic standards. Electrochemical measurements (CV and SWV) were performed by using CH Instruments Electrochemical Analyzer/Workstation Model 660E Series. A standard three-electrode cell was employed with glassy carbon (3 mm diameter) working electrode, a platinum-wire auxiliary electrode, and a saturated calomel electrode (SCE) as reference. All potentials were measured relative to SCE at 298 K and converted to NHE. Controlled potential electrolyses were carried out using platinum mesh as working electrode.

Crystal Structure Determinations: X-ray data were collected on a Bruker SMART APEXII CCD diffractometer, with graphite-monochromated Mo– $K\alpha$ ($\lambda = 0.71073$ Å) radiation. The data for complexes 1 $^{\text{Cl}}$ and 2 $^{\text{Cl}}$ ·MeCN were collected at 100(2) K; whereas for complex 2 $^{\text{ACN}}$ ·0.5MeCN·H $_2$ O the data was collected at 300(2) K. For data

reduction a “Bruker Saint Plus” program was used. Data were corrected for Lorentz and polarization effects; an empirical absorption correction (SADABS v.2.10) was applied. Structures were solved by SIR-2014/SIR-97 and refined by full-matrix least-squares methods based on F^2 using SHELXL-2014/7, incorporated in a WinGX 2014.1 crystallographic collective package.^[33] All non-hydrogen atoms for all the three complexes were refined anisotropically. The positions of all hydrogen atoms were calculated assuming ideal geometries. For 2 $^{\text{Cl}}$ ·MeCN TWIN refinement was performed. The hydrogen atoms of solvent water molecules for 2 $^{\text{ACN}}$ ·0.5MeCN·H $_2$ O could not be assigned due to the poor quality of data. Thus, the refinement of these two oxygen atoms were done without hydrogen atoms joined to them. Pertinent crystallographic parameters are summarized in Table S1 (Supporting Information).

CCDC 1816930 (for 1 $^{\text{Cl}}$), 1816931 (for 2 $^{\text{Cl}}$ ·MeCN), and 1816932 (for 2 $^{\text{ACN}}$ ·0.5MeCN·H $_2$ O) contain the supplementary crystallographic data for this paper. These data can be obtained free of charge from The Cambridge Crystallographic Data Centre.

Kinetic Measurements: The kinetic experiments were carried out spectrophotometrically, using an Agilent 8454 diode array spectrophotometer, equipped with thermostatted cell holder. The temperature of the cell was maintained at 303 K by continuous flow of water connected with a thermostat (Julabo, Model: Corio CD-200F).

Oxygen Evolution Measurements: The Ce^{IV} driven oxidation of water was monitored by an Ocean Optic fluorescence-based oxygen sensor (Neofox-GT, FOSPOR-R) positioned in the headspace of the custom-made glass vessel with a water jacket. The cell temperature was maintained at 303 K by continuous flow of water connected with a thermostat. Two-point calibration was performed under air saturated and nitrogen saturated conditions. The aqueous solution of Ru $^{\text{II}}$ complexes (initial pH 1, $\text{CF}_3\text{SO}_3\text{H}$, 1.8 mL) was taken into the custom made glass vessel. It was sealed with rubber septum and the oxygen needle sensor was inserted through the rubber septum. The solution was deaerated with N_2 gas flow for 20 minutes and then the catalysis was initiated by adding deaerated 0.2 mL of CAN solution [$[\text{catalyst}]_{\text{f}} = 1$ mM, $[\text{CAN}]_{\text{f}} = 60$ mM, total volume of the solution = 2 mL].

Conflicts of Interest

The authors declare no conflicts of interest.

Acknowledgments

Financial support from DST-INSPIRE Faculty award (No. DST/INSPIRE Faculty Award/2012/CH-72) and ISIRD start-up research grant from IIT Kharagpur (No. IIT/SRIC/CHY/SMR/2015-16/60) are gratefully acknowledged. S. M. gratefully acknowledges the research grant from the SERB, New Delhi (EMR/2015/001136) to procure the electrochemical analyser. A. K. and S. D. thank IIT Kharagpur for their Ph.D. fellowship. We thank Central Research Facility (CRF) and Department of Chemistry, IIT Kharagpur for providing the instrumental facilities.

Keywords: Structure elucidation · Ruthenium · Oxidation · Reaction mechanisms

- [1] Paris agreement, 2015, accessed from: http://unfccc.int/files/essential_background/convention/application/pdf/english_paris_agreement.pdf.
- [2] H. Dau, E. Fujita, L. Sun, *ChemSusChem* 2017, 10, 4228–4235.
- [3] M. D. Kärkäs, O. Verho, E. V. Johnston, B. Åkermark, *Chem. Rev.* 2014, 114, 11863–12001.

- [4] X. Sala, S. Maji, R. Bofill, J. Garcia-Anton, L. Escriche, A. Llobet, *Acc. Chem. Res.* **2014**, *47*, 504–516.
- [5] S. W. Gersten, G. J. Samuels, T. J. Meyer, *J. Am. Chem. Soc.* **1982**, *104*, 4029–4030.
- [6] M. D. Kärkäs, B. Åkermark, *Dalton Trans.* **2016**, *45*, 14421–14461.
- [7] a) L. Duan, F. Bozoglian, S. Mandal, B. Stewart, T. Privalov, A. Llobet, L. Sun, *Nat. Chem.* **2012**, *4*, 418–423; b) L. Duan, L. Wang, F. Li, F. Li, L. Sun, *Acc. Chem. Res.* **2015**, *48*, 2084–2096.
- [8] a) A. Draksharapu, Q. Li, H. Logtenberg, T. A. van den Berg, A. Meetsma, J. S. Killeen, B. L. Feringa, R. Hage, G. Roelfes, W. R. Browne, *Inorg. Chem.* **2012**, *51*, 900–913; b) D. Hong, S. Mandal, Y. Yamada, Y.-M. Lee, W. Nam, A. Llobet, S. Fukuzumi, *Inorg. Chem.* **2013**, *52*, 9522–9531.
- [9] Md. A. Asraf, H. A. Younus, M. Yusubov, F. Verpoort, *Catal. Sci. Technol.* **2015**, *5*, 4901–4925.
- [10] P. Garrido-Barros, C. Gimbert-Surinach, R. Matheu, X. Sala, A. Llobet, *Chem. Soc. Rev.* **2017**, *46*, 6088–6098.
- [11] a) K. J. Takeuchi, M. S. Thompson, D. W. Pipes, T. J. Meyer, *Inorg. Chem.* **1984**, *23*, 1845–1851; b) M. Rodriguez, I. Romero, A. Llobet, A. Deronzier, M. Biner, T. Parella, H. Stoeckli-Evans, *Inorg. Chem.* **2001**, *40*, 4150–4156; c) J. J. Concepcion, J. W. Jurss, M. R. Norris, Z. Chen, J. L. Templeton, T. J. Meyer, *Inorg. Chem.* **2010**, *49*, 1277–1279; d) D. J. Wasylenko, C. Ganesamoorthy, M. A. Henderson, B. D. Koivisto, H. D. Osthoff, C. P. Berlinguette, *J. Am. Chem. Soc.* **2010**, *132*, 16094–16106; e) R. Bofill, J. Garcia-Anton, L. Escriche, X. Sala, A. Llobet, *Compr. Inorg. Chem. II* **2013**, *8*, 505–523; f) V. S. Mane, A. S. Kumbhar, R. P. Thummel, *Dalton Trans.* **2017**, *46*, 12901–12907.
- [12] a) C. R. Goldsmith, A. P. Cole, T. D. P. Stack, *J. Am. Chem. Soc.* **2005**, *127*, 9904–9912; b) S. Ohzu, T. Ishizuka, H. Kotani, T. Kojima, *Chem. Commun.* **2014**, *50*, 15018–15021.
- [13] J. Kaizer, E. J. Klinker, N. Y. Oh, J.-U. Rohde, W. J. Song, A. Stubna, J. Kim, E. Munck, W. Nam, L. Que Jr., *J. Am. Chem. Soc.* **2004**, *126*, 472–473.
- [14] J. Chen, Y.-M. Lee, K. M. Davis, X. Wu, M. S. Seo, K.-B. Cho, H. Yoon, Y. J. Park, S. Fukuzumi, Y. N. Pushkar, W. Nam, *J. Am. Chem. Soc.* **2013**, *135*, 6388–6391.
- [15] S. Ohzu, T. Ishizuka, Y. Hirai, H. Jiang, M. Sakaguchi, T. Ogura, S. Fukuzumi, T. Kojima, *Chem. Sci.* **2012**, *3*, 3421–3431.
- [16] a) D. J. Wasylenko, C. Ganesamoorthy, J. Borau-Garcia, C. P. Berlinguette, *Chem. Commun.* **2011**, *47*, 4249–4251; b) K. J. Young, M. K. Takase, G. W. Brudvig, *Inorg. Chem.* **2013**, *52*, 7615–7622.
- [17] a) B. Radaram, J. A. Ivie, W. M. Singh, R. M. Grudzien, J. H. Reibenspies, C. E. Webster, X. Zhao, *Inorg. Chem.* **2011**, *50*, 10564–10571; b) M. Ven-nampalli, G. Liang, C. E. Webster, X. Zhao, *Eur. J. Inorg. Chem.* **2014**, 715–721.
- [18] M. Gil-Sepulcre, M. Bohler, M. Schilling, F. Bozoglian, C. Bachmann, D. Scherrer, T. Fox, B. Spingler, C. Gimbert-Surinach, R. Alberto, R. Bofill, X. Sala, S. Luber, C. J. Richmond, A. Llobet, *ChemSusChem* **2017**, *10*, 4517–4525.
- [19] a) J. J. Concepcion, J. W. Jurss, J. L. Templeton, T. J. Meyer, *J. Am. Chem. Soc.* **2008**, *130*, 16462–16463; b) J. J. Concepcion, M.-K. Tsai, J. T. Muckerman, T. J. Meyer, *J. Am. Chem. Soc.* **2010**, *132*, 1545–1557.
- [20] a) J. Chang, S. Plummer, E. S. F. Berman, D. Striplin, D. Blauch, *Inorg. Chem.* **2004**, *43*, 1735–1742; b) M. H. Al-Sayah, R. McDonald, N. R. Branda, *Eur. J. Org. Chem.* **2004**, 173–182; c) E. Dulière, M. Devillers, J. Marchand-Brynaert, *Organometallics* **2003**, *22*, 804–811.
- [21] M. Okamura, M. Yoshida, R. Kuga, K. Sakai, M. Kondo, S. Masaoka, *Dalton Trans.* **2012**, *41*, 13081–13089.
- [22] a) J. L. Boyer, D. E. Polyansky, D. J. Szalda, R. Zong, R. P. Thummel, E. Fujita, *Angew. Chem. Int. Ed.* **2011**, *50*, 12600–12604; *Angew. Chem.* **2011**, *123*, 12808; b) J. Patel, K. Majee, E. Ahmad, K. Tanaka, S. K. Padhi, *Dalton Trans.* **2015**, *44*, 920–923; c) A. Lewandowska-Andralojc, D. E. Polyansky, R. Zong, R. P. Thummel, E. Fujita, *Phys. Chem. Chem. Phys.* **2013**, *15*, 14058–14068.
- [23] a) M. D. Kärkäs, T. Åkermark, H. Chen, J. Sun, B. Åkermark, *Angew. Chem. Int. Ed.* **2013**, *52*, 4189–4193; *Angew. Chem.* **2013**, *125*, 4283; b) X. Sala, M. Z. Ertem, L. Vigara, T. K. Todorova, W. Chen, R. C. Rocha, F. Aquilante, C. J. Cramer, L. Gagliardi, A. Llobet, *Angew. Chem. Int. Ed.* **2010**, *49*, 7745–7747; *Angew. Chem.* **2010**, *122*, 7911; c) M. D. Kärkäs, Y.-Y. Li, E. M. Siegbahn, R.-Z. Liao, B. Åkermark, *Inorg. Chem.* **2018**, *57*, 10881–10895.
- [24] J. C. Dobson, T. J. Meyer, *Inorg. Chem.* **1988**, *27*, 3283–3291.
- [25] L. Tong, A. K. Inge, L. Duan, L. Wang, X. Zou, L. Sun, *Inorg. Chem.* **2013**, *52*, 2505–2518.
- [26] a) Y. Pushkar, D. Moonshiram, V. Purohit, L. Yan, I. Alperovich, *J. Am. Chem. Soc.* **2014**, *136*, 11938–11945; b) T. Fan, L. Duan, P. Huang, H. Chen, Q. Daniel, M. S. G. Ahlquist, L. Sun, *ACS Catal.* **2017**, *7*, 2956–2966.
- [27] The TON data were also determined at various concentration of complex **2^{Aq}** (0.5 mM & 0.25 mM), using 60 mM of CAN at pH 1. In all cases TONs ≈ 6 are obtained.
- [28] a) Y. Liu, S.-M. Ng, S.-M. Yiu, W. W. Y. Lam, X.-G. Wei, K.-C. Lau, T.-C. Lau, *Angew. Chem. Int. Ed.* **2014**, *53*, 14468–14471; *Angew. Chem.* **2014**, *126*, 14696; b) Y. Liu, G. Chen, S.-M. Yiu, C.-Y. Wong, T. C. Lau, *ChemCatChem* **2018**, *10*, 501–504.
- [29] L. Francàs, X. Sala, E. Escudero-Adan, J. Benet-Buchholz, L. Escriche, A. Llobet, *Inorg. Chem.* **2011**, *50*, 2771–2781.
- [30] A. Gunay, K. H. Theopold, *Chem. Rev.* **2010**, *110*, 1060–1081.
- [31] D. W. Shaffer, Y. Xie, J. J. Concepcion, *Chem. Soc. Rev.* **2017**, *46*, 6170–6193.
- [32] The global analysis, using ReactLab Kinetics version 1.1, was done considering Ce^{IV} and Ce^{III} as non-color species.
- [33] a) G. M. Sheldrick, *Acta Crystallogr., Sect. A* **2015**, *71*, 3–8; b) L. J. Farrugia, WINGX Version **2014.1**. An Integrated Systems of Windows programs for the solution, *Refinement and Analysis of Single-Crystal X-ray Diffraction Data*; Department of Chemistry, University of Glasgow, Glasgow, UK 2014.

Received: September 12, 2018